Nanoscale Advances

ROYAL SOCIETY OF CHEMISTRY

REVIEW

View Article Online
View Journal | View Issue

Cite this: *Nanoscale Adv.*, 2021, **3**, 4370

Element-doped graphitic carbon nitride: confirmation of doped elements and applications

Wenjun Zhang, Datong Xu, Fengjue Wang and Meng Chen *

Received 9th April 2021
Accepted 17th June 2021

DOI: 10.1039/d1na00264c

rsc.li/nanoscale-advances

Doping is widely reported as an efficient strategy to enhance the performance of graphitic carbon nitride (g-CN). In the study of element-doped g-CN, the characterization of doped elements is an indispensable requirement, as well as a huge challenge. In this review, we summarize some useful characterization methods which can confirm the existence and chemical states of doped elements. The advantages and shortcomings of these characterization methods are discussed in detail. Various applications of element-doped g-CN and the function of doped elements are also introduced. Overall, this review article aims to provide helpful information for the research of element-doped g-CN.

1. Introduction

In modern society, energy shortages, environmental issues, and diseases have been prominent problems. To solve these problems, photocatalysts have been developed for different applications, such as hydrogen evolution, pollutant treatment, antibiosis, cancer therapy, and so on.[1–9] Graphitic carbon nitride, a polymeric semiconductor, has become one of the most promising photocatalysts since Wang's group reported this material for hydrogen production from water under visible light.[10] It should be noted that graphitic carbon nitride is often wrongly named "g-C_3N_4" in the literature, but "perfect" g-C_3N_4 has not been synthesized so far.[11] Therefore, we decided to denote graphitic carbon nitride as "g-CN" in this review.

Up to now, g-CN, which is a low-cost, non-toxic, and environment-friendly material, has been a star photocatalyst because of its simple synthesis, tunable bandgap, and visible-light absorption.[12] g-CN can be facilely prepared *via* thermal condensation of nitrogen-rich precursors, such as urea, thiourea, cyanamide, dicyandiamide, and melamine.[13,14] The bandgap of g-CN is ~2.7 eV with the conduction band (CB) minimum at ~−1.1 eV and the valence band (VB) maximum at ~+1.6 eV *vs.* normal hydrogen electrode (NHE).[15,16] Such an energy band structure allows g-CN to absorb visible light and provide active groups for reactions. However, pristine g-CN suffers from several disadvantages including the low specific surface area, narrow optical absorption range, and high recombination efficiency of charge carriers,[17–19] which limit the practical applications of g-CN. Therefore, tremendous efforts have been made to overcome the limitations mentioned above, including the preparation of g-CN-based composites, modification of precursors, post-treatment of g-CN, exfoliation, element doping, and so on.[20–29]

Element doping is a potential strategy to enhance the performance of g-CN, thus the doping of various elements has

Department of Materials Science, Fudan University, Shanghai 200433, PR China. E-mail: chenmeng@fudan.edu.cn

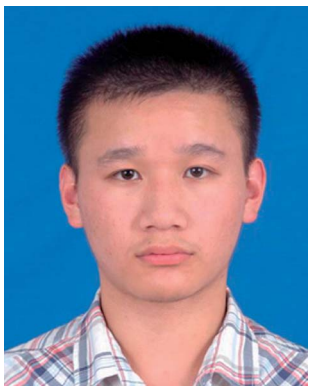

Wenjun Zhang was born in May 1994. He received his Bachelor's degree from the School of Materials Science and Engineering from Zhejiang University (2016). Now, he is studying for a Master's degree at Fudan University. His research interest is the modification of the photocatalytic performance of carbon nitride.

Datong Xu was born in October 1997. He received his Bachelor's degree in Polymer Materials and Engineering from Nantong University (2019). Now, he is studying for a Master's degree at Fudan University. His research interest is the modification of the photocatalytic performance of carbon nitride.

been reported in recent years. Different from g-CN-based composites, element-doped g-CN always involves the changes in the microstructure of g-CN, such as the loss of the graphitic structure[30] and the impact on the in-plane ordering of tri-*s*-triazine units.[31] Therefore, accurate characterization results are required to determine the existence of heteroatoms in element-doped g-CN.

In this review, we focus on the characterization methods that can provide evidence of successful element doping in g-CN. Relevant characterization techniques and their functions, namely how they can determine the doping of exotic elements will be discussed. Furthermore, the applications of element-doped g-CN will be introduced to show the positive influence of dopants on the performance of element-doped g-CN.

2. Confirmation of doped elements in g-CN

As the dopants in element-doped g-CN cannot be observed directly in electron microscopy images, comprehensive characterization methods should be applied to confirm the presence and chemical states of doped elements. The advantages and shortcomings of the techniques that can be used for the characterization of element-doped g-CN will be discussed below. Furthermore, the effect of doped elements on the band structure of g-CN will also be introduced because of the importance of band structure to the performance of g-CN materials.

2.1 X-ray photoelectron spectroscopy

X-ray photoelectron spectroscopy (XPS) measurements are widely used in the characterization of non-metallic element-doped g-CN. The oxidation states of the doped elements are understood by the XPS peak positions in their core-level spectra; therefore, the bond types of heteroatoms are determined. For example, Wang's group obtained fluorine-doped g-CN (F/g-CN) by evaporating the mixed precursor solution of dicyandiamide and NH_4F and then calcining the resultant solid.[31] A peak at 686.2 eV is shown in the XPS spectrum of F 1s (Fig. 1(a)), which can be assigned to the C–F bonds according to the previous report.[34] Therefore, the XPS results indicate that F atoms are successfully introduced into the g-CN matrix as C–F bonds. Similar conclusions are also reported by other research groups.[35–37] Doping of other non-metallic elements, such as B,[38–48] P,[49–59] S,[60–66] and so on, can also be characterized by XPS measurements.

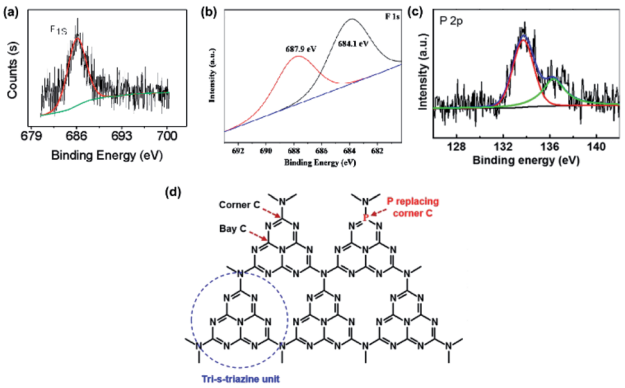

Fig. 1 (a) F 1s XPS spectrum of F/g-CN. Reprinted with permission from ref. 31, copyright 2010, American Chemical Society. (b) F 1s XPS spectrum of F/g-CN. Reprinted with permission from ref. 32, copyright 2018, Elsevier. (c) P 2p XPS spectrum of P/g-CN and (d) illustration of replacement of corner C by P. Reprinted with permission from ref. 33, copyright 2018, Elsevier.

Although the bond types of heteroatoms can be easily determined by the XPS peak positions, these characteristic peaks can be affected by some factors. The work of Chew's group, which prepared F/g-CN *via* the hydrothermal treatment of g-CN with NH_4F, indicated that the XPS peak positions of C–F bonds can be altered by the strength of bonds.[32] The XPS spectrum of their sample is shown in Fig. 1(b). The XPS peaks in

Fengjue Wang was born in December 1998. She received her B.E. degree in Composite Materials from Wuhan University of Technology (2020). Then, she joined the Department of Materials Science, Fudan University as a MA.Sc candidate. Her scientific interests cover the preparation and composites of two-dimensional nanomaterials and the performance of photocatalysis.

Meng Chen obtained his PhD in Inorganic Chemistry from University of Science and Technology of China, Hefei, P. R. China. Currently, he is working as an Associate Professor at the Department of Materials Science, Fudan University, Shanghai, P. R. China. He took two terms of postdoctoral research about nanomaterials at Clemson University and Rice University. His research interests include the synthesis and characterization of low-dimensional structure materials and their applications in photocatalytic water splitting, and degradation of organic pollutants. He has authored and co-authored over 50 peer-reviewed articles published in leading international scientific journals.

the F 1s spectrum are divided into two components due to binding strength. One peak at 684.1 eV, whose binding energy is lower, is attributed to the weak bonds of isolated F atoms with C atoms; the other peak at 687.9 eV, whose binding energy is higher, is attributed to covalent C–F bonds. Another research shows that the doping position of heteroatoms can lead to some special XPS peaks.[33] A new peak at 136.3 eV appears in the XPS spectrum of P-doped g-CN (Fig. 1(c)), which is quite different from the value of P–N bonds (133.7 eV) or P–C bonds (~1–2 eV lower than that of P–N bonds). This peak can be attributed to the replacement of corner C atoms by P atoms (Fig. 1(d)) according to the computation results of the in-planar distance of nitride pores.

XPS measurements are also applicable to verify the doping of metallic elements in element-doped g-CN, such as Fe,[30,67–75] Co,[76–80] Mn,[76,81–83] and so on. But, unlike the replacement of C or N atoms by non-metallic elements, metallic elements tend to anchor to the cavities between tri-*s*-triazine units and form coordination bonds with N atoms (Fig. 2).[77,84–88] Hence, the characteristic peak positions of metallic elements correspond to their valence states. For instance, Fe is one of the commonest elements used in g-CN doping. Typically, Fe-doped g-CN (Fe/g-CN) can be synthesized *via* evaporating the mixed precursor solution of dicyandiamide and ferric salt and then calcining the resultant solid.[30,67,70,71] The XPS spectra of Fe in Fe/g-CN are shown in Fig. 3. The XPS peak of Fe $2p_{3/2}$ at ~710.5 eV, which lies within the range of the binding energy of Fe^{3+} valence state (710.3–711.8 eV),[89] indicates the presence of Fe^{3+} in Fe/g-CN. Fe^{3+} can also exist in the composites of g-CN and iron species,[90] so more evidence of doping should be provided: the absence of iron species can be observed *via* the X-ray diffraction (XRD) patterns of Fe/g-CN samples;[30] elemental mapping is also utilized to display the uniform distribution of Fe atoms in Fe/g-CN, namely the successful doping of Fe.[91]

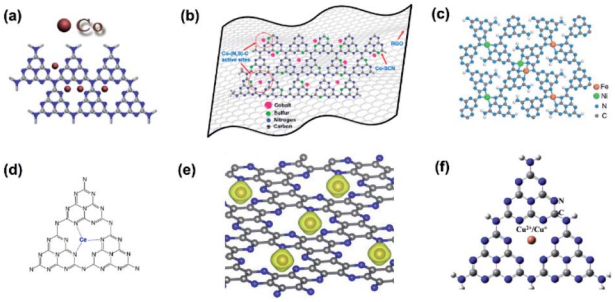

Fig. 2 (a) Chemical structure of Co-doped g-CN. Reprinted with permission from ref. 77, copyright 2019, Elsevier. (b) Chemical structure of Co-coordinated S-doped g-CN on reduced graphene oxide (RGO). Reprinted with permission from ref. 84, copyright 2019, American Chemical Society. (c) Chemical structure of Fe–Ni co-doped g-CN. Reprinted with permission from ref. 85, copyright 2019, Royal Society of Chemistry. (d) Chemical structure of Ce-doped g-CN. Reprinted with permission from ref. 86, copyright 2015, Wiley. (e) Chemical structure of 3d transition-metal doped g-CN (the yellow balls represent Fe, Co, and Ni atoms). Reprinted with permission from ref. 87, copyright 2017, Elsevier. (f) Chemical structure of Cu^{2+}/Cu^{+} doped g-CN. Reprinted with permission from ref. 88, copyright 2018, Elsevier.

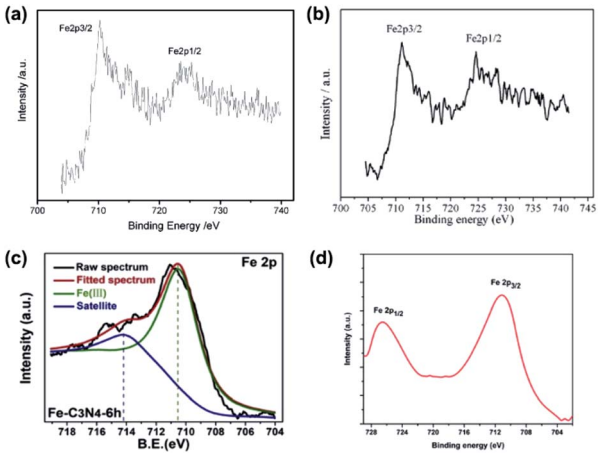

Fig. 3 (a) XPS spectra of Fe in Fe/g-CN. Reprinted with permission from ref. 30, copyright 2009, Wiley. (b) XPS spectra of Fe in Fe/g-CN. Reprinted with permission from ref. 70, copyright 2010, Elsevier. (c) XPS spectra of Fe in Fe/g-CN. Reprinted with permission from ref. 67, copyright 2020, Elsevier. (d) XPS spectra of Fe in Fe/g-CN. Reprinted with permission from ref. 71, copyright 2014, Royal Society of Chemistry.

To facilitate further research on g-CN doping, we summarize the reported bond types or oxidation states of heteroatoms and their XPS peak positions in element-doped g-CN materials in Table 1, thus the doping condition of a novel g-CN-based material can be quickly determined.

2.2 Nuclear magnetic resonance

Nuclear magnetic resonance (NMR) is a powerful technique applied for the characterization of non-metallic element-doped g-CN. Peaks in NMR spectra reflect the chemical environment of a doped element, thus the chemical structure of element-doped g-CN can be speculated. B-doped carbon nitride microspheres (B-SSCN) were synthesized by Xue's group *via* a one-pot solvothermal method using ammonia borane, cyanuric chloride, and cyanuric acid as precursors.[41] The ^{11}B solid-state NMR spectrum of B-SSCN is shown in Fig. 4(a). The peaks at 15.9 and 6.72 ppm are considered as the result of sp^2-coordinated B at the bay and corner C sites in the tri-*s*-triazine rings, and the peak at 2.97 ppm can be assigned to sp^3-coordinated borane such as $BH(N_3)$.[159–161] These results suggest that B atoms have been successfully doped into the microstructure of g-CN (Fig. 4(b)). Similar results are also discussed by Wang's group (Fig. 4(c)).[40] The NMR spectra and proposed microstructures of some other element-doped g-CN materials are also determined by researchers (Fig. 4(d) and (e)).[31,50]

Notably, some structural details can be obtained *via* NMR, while other characterization methods have a limited effect. NMR can be used to determine the doping of oxygen, which widely exists on the surface of pristine g-CN,[162] thus it becomes difficult to confirm the presence of O atoms in the microstructure of g-CN. Sun's group prepared O-doped g-CN (O–CN) *via* the solvothermal treatment of g-CN with cyanuric chloride.[92] To prove the existence of O atoms in the microstructure of g-CN,

Table 1 Possible bond types or oxidation states of heteroatoms and their XPS peak positions in element-doped g-CN materials

Element	Bond type or oxidation state	XPS peak (eV)	Ref.
B	B–N	190.8	38
	B–N–C	191.1–192.4	39–44
	B–N–C_2	190.1	44
	B–C_3	190.9	45 and 46
	B–C_2O	191.8	45 and 46
	N–B–N	191.7	47 and 48
	B–O	192.3	44
F	C–F_2	692.0	37
	Weak C–F bonds	684.1	32
	Covalent C–F bonds	687.9	32
O	C–O–C	531.5–533.2	92 and 93
	C═O	532.3	93
	N–C–O	531.45	94
Na	Na^+	1070.3–1071.7	59 and 95–98
Mg	Mg^{2+}	305.2 (Auger)	99
Al	Al^{3+}	76.0 (Al $2p_{3/2}$)	100
		72.1 (Al $2p_{1/2}$)	
Si	Si–N	102.2–102.8	101
P	P═N	132.8	49
	P–N	133.3–134.0	49–54, 56 and 59
	P–C	131.5–132.6	50, 55 and 58
	P–O–C	133.5	57
	P–O	136.0	57
	Replacement of corner C by P	136.3	33
S	C–S–C	161.8–164.0	60, and 62–66
	S–C–N	165.6	63
	S–N	165.4	66
	S–O	168.0	62
	C–S	165.4 (S $2p_{3/2}$)	61
		164.3 (S $2p_{1/2}$)	
Cl	Cl–N	197.6–198.1 (Cl $2p_{3/2}$)	102 and 103
		199.5–200.0 (Cl $2p_{1/2}$)	
K	K^+	295.2–295.5 (K $2p_{3/2}$)	104–110
		292.5–293.1 (K $2p_{1/2}$)	
Ti	Ti^{4+}	457.4 (Ti $2p_{3/2}$)	111
		462.8 (Ti $2p_{1/2}$)	
V	V^{4+-5+}	516.7 (V $2p_{3/2}$)	112
		524.1 (V $2p_{1/2}$)	
Cr	Cr^{2+}	575.7–575.9 (Cr 2p)	113
	Cr^{3+}	576.7–577.2 (Cr 2p)	113
	Cr^{6+}	578.2–579.3 (Cr 2p)	113
Mn	Mn^{2+}	640.8–641.3 (Mn $2p_{3/2}$)	81 and 82
		653.3 (Mn $2p_{1/2}$)	
	Mn^{3+}	639.5–642.1 (Mn $2p_{3/2}$)	76, 82 and 83
		651.7–652.7 (Mn $2p_{1/2}$)	
	Mn^{4+}	646.5 (Mn $2p_{3/2}$)	83
		656.4 (Mn $2p_{1/2}$)	
Fe	Fe^{2+}	709.2–715.9 (Fe $2p_{3/2}$)	67–69
		723.7 (Fe $2p_{1/2}$)	
	Fe^{3+}	710.3–711.8 (Fe $2p_{3/2}$)	30, 67, 68, 70–75 and 114
		723.9–725.7 (Fe $2p_{1/2}$)	
Co	Co^{3+}	781.2–782.5 (Co $2p_{3/2}$)	76–80
		797.0–799.0 (Co $2p_{1/2}$)	
Ni	Ni^{2+}	853.5 (Ni $2p_{3/2}$)	115
		859.2 (Ni $2p_{1/2}$)	
	Ni^{3+}	855.8–856.1 (Ni $2p_{3/2}$)	76 and 116
		873.2–874.1 (Ni $2p_{1/2}$)	
Cu	Cu^+	932.1–932.8 (Cu $2p_{3/2}$)	117–119
		951.9–952.6 (Cu $2p_{1/2}$)	
	Cu^{2+}	932.5–933.3 (Cu $2p_{3/2}$)	76, 117, 120 and 121
		959.1–953.3 (Cu $2p_{1/2}$)	
Zn	Zn^{2+}	1022.1–1022.4 (Zn $2p_{3/2}$)	122 and 123
		1045.1–1045.4 (Zn $2p_{1/2}$)	

Table 1 (*Contd.*)

Element	Bond type or oxidation state	XPS peak (eV)	Ref.
Se	Se–C	53.8–57.8	124–126
	$Se{=}C(NH_2)_2$	55.0	124
	Se–N	52.3–53.4	125 and 126
Br	Br^-	67.5–67.6 (Br $3d_{5/2}$) 68.3–68.5 (Br $3d_{5/2}$)	127 and 128
	Br–C	68.3–69.3	127, 129 and 130
Sr	Sr^{2+}	133.4 (Sr $3d_{5/2}$) 135.0 (Sr $3d_{3/2}$)	131
Y	Y^{3+}	154.6 (Y $3d_{5/2}$) 159.7 (Y $3d_{3/2}$)	132
Zr	Zr^{4+}	181.6 (Zr $3d_{5/2}$) 184.0 (Zr $3d_{3/2}$)	133
Mo	Mo^{6+}	231.8–232.1 (Mo $3d_{5/2}$) 235.1–235.3 (Mo $3d_{3/2}$)	134–137
Pd	Pd^{2+}	338.3 (Pd $3d_{5/2}$) 343.6 (Pd $3d_{3/2}$)	138
In	In^{3+}	445.1 (In $3d_{5/2}$) 452.6 (In $3d_{3/2}$)	139
Sb	Sb^{3+}	530.6 (Sb $3d_{5/2}$) 539.9 (Sb $3d_{3/2}$)	140
Te	Te^{4+}	575.0 (Te $3d_{5/2}$) 585.5 (Te $3d_{3/2}$)	141
	Te^{6+}	577.0 (Te $3d_{5/2}$) 588.0 (Te $3d_{3/2}$)	141
I	C–I	617.8–619.3 (I $3d_{5/2}$) 629.8–630.7 (I $3d_{3/2}$)	142–146
	$C–I^+–C$	619.8–619.9 (I $3d_{5/2}$)	142 and 144–146
Ba	Ba^{2+}	779.6–780.1 (Ba $3d_{5/2}$) 795.0–795.4 (Ba $3d_{3/2}$)	147 and 148
La	La^{3+}	834.3 and 837.8 (La $3d_{5/2}$) 851.4 and 854.5 (La $3d_{3/2}$)	149
Ce	Ce^{3+}	882.3, 885.6–886.0, and 888.4 (Ce $3d_{5/2}$) 899.4–900.8, 904.4, and 907.3 (Ce $3d_{3/2}$)	150–152
	Ce^{4+}	881.9–882.4, 885.7, and 888.4 (Ce $3d_{5/2}$) 900.5–900.8, 904.1, 907.2, and 916.3 (Ce $3d_{3/2}$)	150–152
Sm	Sm^{3+}	1084.0 (Sm $3d_{5/2}$) 1105.0 (Sm $3d_{3/2}$)	153
Eu	Eu^{3+}	1124.3 and 1135.8 (Eu $3d_{5/2}$) 1165.6 (Eu $3d_{3/2}$)	154
Gd	Gd^{3+}	142.4 and 148.8 (Gd $4d_{5/2}$) 171.0 (Gd $4d_{3/2}$)	155
Er	Er^{3+}	167.0–171.0 (Er $4d_{5/2}$)	156
Pt	Pt^{2+}	73.0–73.3 (Pt $4f_{7/2}$) 76.4–76.5 (Pt $4f_{5/2}$)	157 and 158

solid-state ^{13}C NMR spectra of pristine g-CN (CN), composite of O–CN and CN (O–CN/CN-3), and O–CN were obtained (Fig. 4(f)). Compared with CN, O–CN shows a unique peak at 163.3 ppm, which is attributed to the replacement of NH_x species by O atoms.[163] This result suggests that O atoms have been introduced into g-CN. Furthermore, NMR measurements are beneficial to discover the special chemical environment of doped elements. Tao's group synthesized P-doped g-CN (PCN) *via* annealing the mixed precursor of phytic acid and urea and then prepared P-doped g-CN nanoflakes (PCNNFs) *via* the post-treatment of PCN.[33] The ^{31}P NMR spectra of PCN and PCNNFs are shown in Fig. 4(g). Two peaks at −28.1 and −41.3 ppm, which only exist in the spectrum of PCNNFs, can be attributed to the terminal P species formed in the process of preparing PCNNFs.

2.3 Fourier transform infrared spectroscopy

Typically, with the introduction of non-metallic heteroatoms, some new vibration modes may be created, or some inherent vibration modes may be influenced. Therefore, Fourier transform infrared spectroscopy (FTIR) measurements can be used in the characterization of non-metallic element-doped g-CN materials. For example, Huang's group prepared Cl-doped g-CN *via* the thermal treatment for the mixed precursor of melamine and cyanuric chloride.[164] Fig. 5(a) shows the FTIR spectra of bulk g-CN (sample I) and Cl-doped g-CN (samples II and III). A

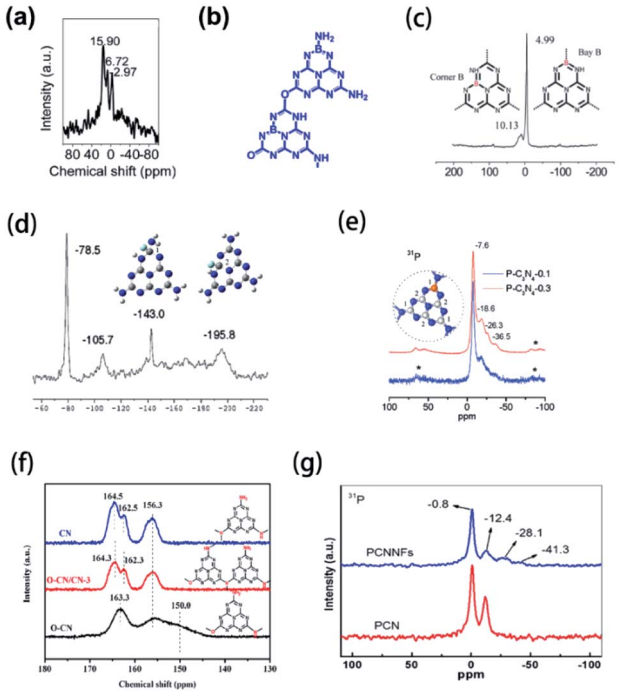

Fig. 4 (a) ^{11}B NMR spectrum and (b) microstructure of B-SSCN. Reprinted with permission from ref. 41, copyright 2016, Wiley. (c) ^{11}B NMR spectra and microstructures of B-doped g-CN. Reprinted with permission from ref. 40, copyright 2011, Royal Society of Chemistry. (d) ^{19}F NMR spectrum and microstructures of F-doped g-CN (blue, grey, white, and green balls represent N, C, H, and F atoms, respectively). Reprinted with permission from ref. 31, copyright 2010, American Chemical Society. (e) ^{31}P NMR spectra and microstructure of P-doped g-CN (blue, grey, and orange balls represent N, C, and P atoms, respectively). Reprinted with permission from ref. 50, copyright 2010, American Chemical Society. (f) ^{13}C NMR spectra and microstructures of CN, O–CN/CN-3, and O–CN. Reprinted with permission from ref. 92, copyright 2020, Elsevier. (g) ^{31}P NMR spectra of PCN and PCNNFs. Reprinted with permission from ref. 33, copyright 2018, Elsevier.

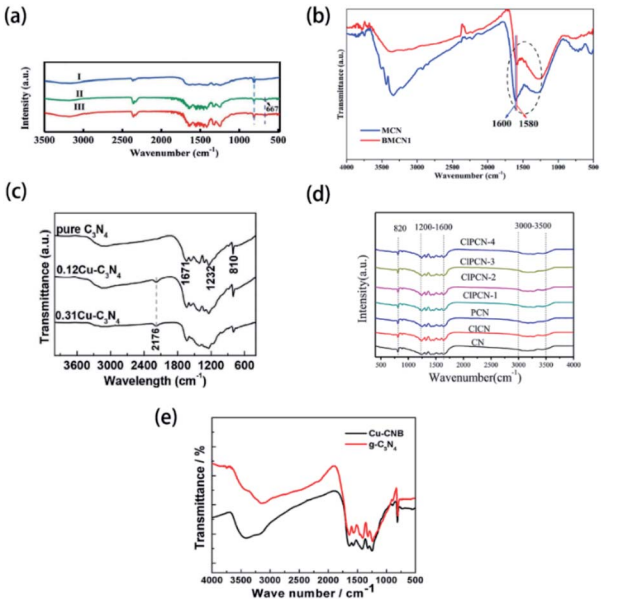

Fig. 5 (a) FTIR spectra of bulk g-CN(I) and Cl-doped g-CN (II & III). Reprinted with permission from ref. 164, copyright 2019, Elsevier. (b) FTIR spectra of mesoporous g-CN (MCN) and B-doped mesoporous g-CN (BMCN). Reprinted with permission from ref. 165, copyright 2019, Elsevier. (c) FTIR spectra of pure g-CN, 0.12Cu–C_3N_4, and 0.31Cu–C_3N_4. Reprinted with permission from ref. 119, copyright 2015, Elsevier. (d) FTIR spectra of g-CN (CN), Cl-doped g-CN (ClCN), P-doped g-CN (PCN), and P–Cl co-doped g-CN (ClPCN-1–ClPCN-4). Reprinted with permission from ref. 103, copyright 2020, Elsevier. (e) FTIR spectra of g-CN and Cu and B co-doped g-CN (Cu-CNB). Reprinted with permission from ref. 170, copyright 2015, MDPI.

new vibration band at ~667 cm^{-1} exists only in the spectra of samples II and III, which is related to the stretching vibration of C–Cl and thus implies the successful doping of Cl atoms. But, in the FTIR spectra of some samples, instead of the appearance of the new bands, doped elements can influence the characteristic band positions. As shown in Fig. 5(b), the FTIR spectra of mesoporous g-CN (MCN) and B-doped mesoporous g-CN (BMCN) prepared by Badiei's group are consistent except for the band at 1600 cm^{-1} or MCN slightly shifting to 1580 cm^{-1} or BMCN, which suggests that B doping changed the tri-*s*-triazine units.[165] Herein, we collect the data of the reported bond types related to the doped elements in g-CN and their characteristic FTIR bands in Table 2.

Interestingly, though the vibration modes of metal-contained bonds are unable to be reflected in FTIR spectra, the doping of metallic elements can result in some new vibration modes and further suggest the successful doping of heteroatoms. Asefa's group reported the synthesis of Cu-doped g-CN (Cu-C_3N_4) *via* annealing the mixed precursor of copper(II) salt and dicyandiamide.[119] As shown in Fig. 5(c), the new band of Cu-C_3N_4 at 2176 cm^{-1}, which is assigned to the stretching mode of the C≡N bond, demonstrates that the doping of Cu atoms leads to the formation of defect sites.[88,171]

However, FTIR spectroscopy suffers the following disadvantages in the characterization of element-doped g-CN: (1) according to some reports, doping may make no difference between the FTIR spectra of pristine g-CN and element-doped g-CN because the heteroatoms do not change the microstructure of g-CN;[38,42,56,62,64,66] (2) FTIR bands can be influenced by the content of heteroatoms. Yang's group synthesized P–Cl co-doped g-CN *via* annealing the mixed precursor of ammonium chloride, ammonium phosphate, and melamine.[103] The FTIR spectra of their samples exhibit bands at 820, 1200–1600 and 3000–3500 cm^{-1}, which are attributed to the breathing mode of tri-*s*-triazine rings, stretching vibration modes of CN heterocycles, and uncondensed terminal amino groups, respectively; while no vibration bands associated with P or Cl groups are discovered due to the low content of P and Cl (Fig. 5(d)). (3) FTIR bands of doped elements may not appear due to overlapping. Han's group prepared Cu and B co-doped g-CN (Cu-CNB) *via* calcining the mixed precursor of 1-cyanopropyl-3-methylimidazolium tetrafluoroborate, $Cu(NO_3)_2 \cdot 3H_2O$, and urea.[170] The FTIR spectra of g-CN and Cu-CNB are shown in Fig. 5(e). The typical vibration bands of B–N bonds should appear at 1370 cm^{-1}, but they were presumably overlapped by the C–N stretching vibrations.[172] The FTIR spectra of B-doped g-CN

Table 2 Possible bond types of heteroatoms and the positions of their FTIR band in element-doped g-CN materials

Element	Bond type	FTIR band (cm^{-1})	Ref.
B	B–N	1370–1398 (stretching vibration)	41, 43, 48 and 166
Cl	C–Cl	667 (stretching vibration)	164
F	C–F	1220 (stretching vibration)	31, 35 and 166
I	C–I	539.9 (stretching vibration)	143
P	P–N	502 (bending vibration)	51 and 167
		950 (stretching vibration)	
	P–OH	978 (stretching vibration)	167
S	C–S	1050–1200 (stretching vibration)	64 and 168
	C═S	1126–1185 (stretching vibration)	61 and 169
	S–H	2380–2400 (stretching vibration)	168
Se	Se–N	2250 (stretching vibration)	124
Si	Si–N	760 (stretching vibration)	101

samples prepared by other research groups also showed the same result.[48,173]

2.4 X-ray absorption spectroscopy

X-ray absorption spectroscopy (XAS) measurements, including X-ray absorption near-edge structure (XANES), near-edge X-ray absorption fine structure (NEXAFS) and extended X-ray absorption fine structure (EXAFS), can be used to characterize the chemical states of doped elements in g-CN-based materials.[60,85,114,174,175] The bond types of doped elements can be easily distinguished according to EXAFS peaks. For instance, as shown in the Fourier-transformed EXAFS (FT-EXAFS) spectra (Fig. 6(a)), a novel peak of Fe–g-CN at 1.54 Å implies the back-scattering of the first coordination shell of Fe–N bonds.[174] To gain more insight, the oxidation states of doped elements can be determined *via* XANES spectra in Fig. 6(b): the normalized Fe K-edge XANES spectra of Fe-g-CN, Fe_2O_3, and the reference Fe foil were measured. The absorption edge of Fe-g-CN possesses higher energy than Fe_2O_3 and lower energy than the Fe foil, which indicates that the oxidation state of Fe in the sample is between Fe(0) and Fe^{3+}. Based on the evidence shown above, they proved the successful doping of Fe atoms. Similar methods were also used in the characterization of other element-doped g-CN. Sun's group prepared Ni-doped g-CN (Ni@PCN) and Ni-Fe co-doped g-CN (NiFe@PCN) for the oxygen evolution reaction.[85] FT-EXAFS spectra of these samples are shown in Fig. 6(c); the peak of both Ni@PCN and $Ni_{0.65}Fe_{0.35}$@PCN at 1.8 Å corresponds to the Ni–N bond, which indicates the doping of Ni in these samples. Liu's group synthesized S-doped g-CN, and the S K-edge XANES spectrum of this material is shown in Fig. 6(d).[60] Two pre-edge features at 2472.6 and 2482.0 eV can be assigned to two kinds of functional groups, $S^{\theta-}$ ($0 < \theta \leq 2$) and SO_4^{2-}, respectively. $S^{\theta-}$ species is the result of the replacement of N atoms with S atoms, namely the formation of C–S bond; SO_4^{2-} species exist on the surface of S-doped g-CN.

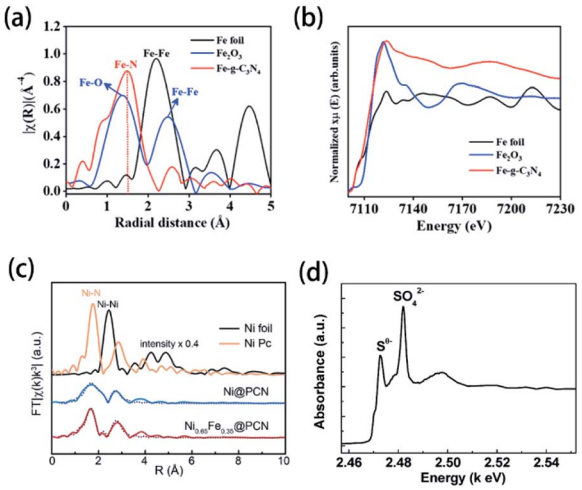

Fig. 6 (a) FT-EXAFS spectra and (b) Fe K-edge XANES spectra of the Fe foil, Fe_2O_3, and Fe-g-CN. Reprinted with permission from ref. 174, copyright 2020, American Chemical Society. (c) FT-EXAFS spectra of the Ni foil, Ni Pc, Ni@PCN, and $Ni_{0.65}Fe_{0.35}$@PCN. Reprinted with permission from ref. 85, copyright 2019, Royal Society of Chemistry. (d) S K-edge XANES spectrum of S-doped g-CN. Reprinted with permission from ref. 60, copyright 2010, American Chemical Society.

Compared with other characterization techniques, XAS measurement is considered a more powerful and efficient technique to gain direct insights into the chemical environments of target atoms. In general, XAS measurement exhibits the following advantages:[176] (1) fitting to the investigation of amorphous materials; (2) potent detection at a low concentration; and (3) high spatial and temporal resolutions for an *in situ* experiment. Hence, XAS has been extensively utilized in the study of materials science in recent years,[182,183] especially in the research of some element-doped materials, such as Cu-exchanged zeolites,[184] P-doped hematite,[185] Ta-doped α-Fe_2O_3 nanorods,[186] and P–B co-doped amorphous porous Ni–Fe-based material.[187] Therefore, the future looks bright for the use of XAS measurement in the characterization of element-doped g-CN, though very little work about this has been carried out so far.

2.5 Elemental mapping and electron energy-loss spectroscopy

Elemental mapping is suitable for the characterization of element-doped g-CN. Generally, the uniform distribution of the target element can be directly observed in elemental mapping results, which demonstrates the successful doping combined with the absence of nanoparticles in electron microscopy

images. The vast majority of doped elements, such as Cu (Fig. 7(a–c)),[88] S (Fig. 7(d–f)),[177] F (Fig. 7(g)),[35] Ce (Fig. 7(h–i)),[86] and so on, can be characterized easily by elemental mapping. However, it is noteworthy that we can only confirm the 'existence' of elements but not the 'doping' of elements through elemental mapping. For example, as shown in Fig. 7(j–m), the uniform distribution of Co can also be observed in the elemental mapping results of a co-catalyst system containing g-CN and the cobalt-based cubane molecular, which is not an element-doped g-CN material.[178] Therefore, more characterization information, such as electron microscopy images and the characterization techniques mentioned above, has to be provided to certify the successful doping.

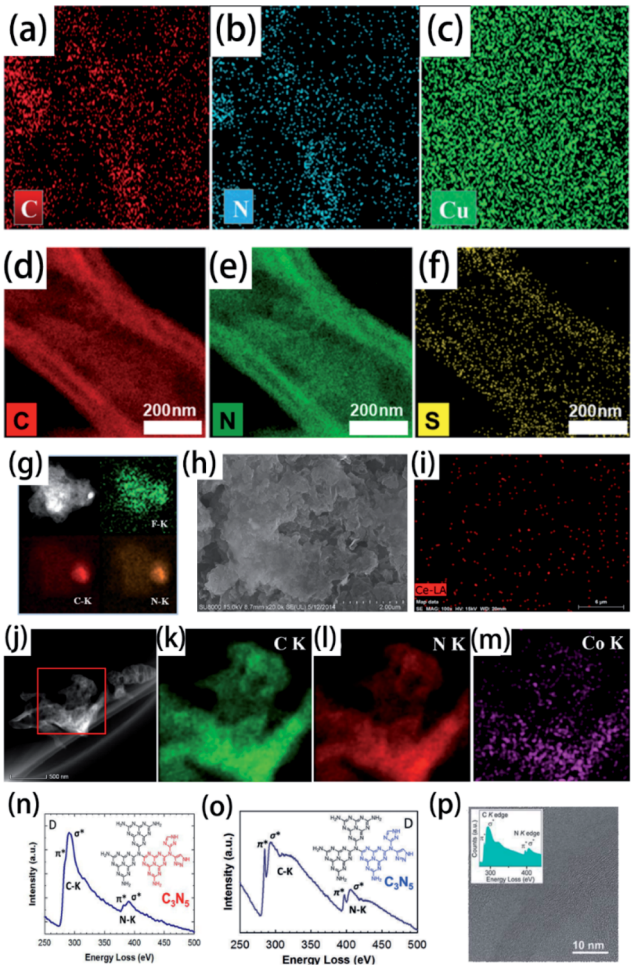

Fig. 7 Elemental mapping images of (a) C, (b) N, and (c) Cu for Cu^{2+}-doped g-CN. Reprinted with permission from ref. 88, copyright 2018, Elsevier. Elemental mapping images of (d) C, (e) N, and (f) S for S-doped g-CN. Reprinted with permission from ref. 177, copyright 2020, Elsevier. (g) Elemental mapping images of F, C, and N for F-doped g-CN nanosheets. Reprinted with permission from ref. 35, copyright 2015, Royal Society of Chemistry. (h) SEM image of Ce-doped g-CN and (i) elemental mapping image of Ce for this material. Reprinted with permission from ref. 86, copyright 2015, Wiley. (j) HAADF-STEM image of cobalt-based cubane molecular and g-CN co-catalysts and elemental mapping images of (k) C, (l) N, and (m) Co for this material. Reprinted with permission from ref. 178, copyright 2018, Elsevier. (n) EELS spectrum of highly ordered mesoporous C_3N_5. Reprinted with permission from ref. 179, copyright 2017, Wiley. (o) EELS spectrum of highly ordered nitrogen-rich mesoporous C_3N_5. Reprinted with permission from ref. 180, copyright 2017, Wiley. (p) EELS of g-CN. Reprinted with permission from ref. 181, copyright 2011, Royal Society of Chemistry.

Electron energy-loss spectroscopy (EELS) is another available tool for elemental analysis. EELS is especially useful for the analysis of light elements, and its spatial resolution is higher than that of elemental mapping, meaning that it is particularly suitable for the detection of doped elements.[188] This technique has been widely used in the elemental analysis of carbon nitride materials.[179–181] As shown in (n–p), the characteristic peaks in the EELS spectra illustrate the presence of C and N in g-CN and C_3N_5. Therefore, we believe that EELS can also be applied for the characterization of element-doped g-CN—although it is rarely used in the research of element-doped g-CN nowadays.

2.6 Band structure

It is well known that the band structure has a decisive impact on the properties of g-CN materials. Therefore, it is very necessary to mention the effect of element doping on the band structure of g-CN. The values of the CB minimum, VB maximum, and band gap are the most important information about the band structure of element-doped g-CN. Generally, the value of the band gap can be determined *via* UV-vis diffuse reflectance spectroscopy (DRS).[37,102,132] The values of the CB minimum and VB maximum can be evaluated using Mott–Schottky plots or XPS valence band spectra.[44,78,94,154]

As the situations of non-metallic element and metallic element doping are quite different, they will be discussed separately in this section. According to related research results, the influence of diverse non-metallic elements doping on the band structure varies greatly. As shown in Fig. 8(a), the majority of non-metallic element-doped g-CN possess a narrower band gap than that of pristine g-CN, which makes them have better optical absorption ability and thus more excellent photocatalytic performance.[38,55,62,130] Such a change of band gap can be attributed to the following reasons: (1) defects are formed during the synthesis process due to the doping of elements, which can enhance the optical absorption[38] and (2) doped elements lead to electronic integration, which can also influence the band gap.[50,62] Fig. 8(a) also illustrates that the VB and CB positions of different non-metallic element-doped g-CN materials are located in a wide range, which may be ascribed to the electronegativity difference among C, N, and doped elements.[44,60] Sometimes, this variation of VB and CB positions can cause a wider band gap.[101,103]

The band structures of some metallic element-doped g-CN materials are shown in Fig. 8(b). Although their VB and CB positions are various, all of their band gaps are narrower than that of pristine g-CN. The charge-transfer transition between the electrons of the doped metallic element and the VB or CB of g-CN can result in the redshift of absorption edge in the DRS spectrum of a metallic element-doped g-CN material, which means the narrower band gap.[132] In addition, the doping of metallic elements can produce a midgap state in the band gap. The midgap state can hold the electrons that are photo-excited

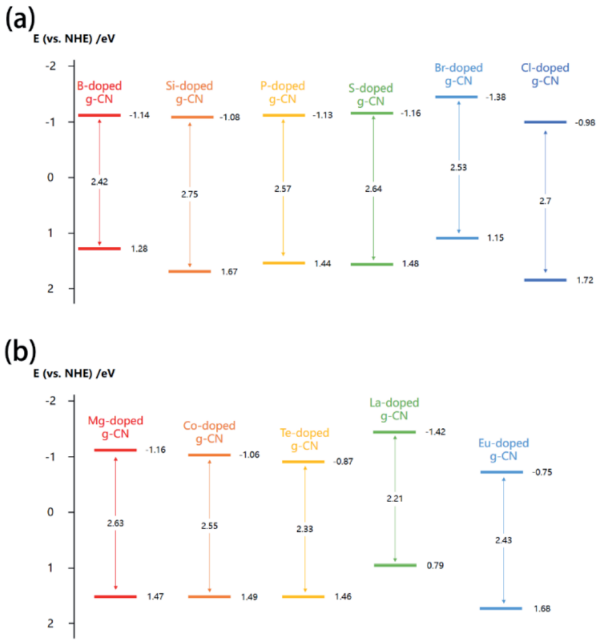

Fig. 8 (a) Band structures of B-doped g-CN from ref. 38, Si-doped g-CN from ref. 101, P-doped g-CN from ref. 55, S-doped g-CN from ref. 62, Br-doped g-CN from ref. 130, and Cl-doped g-CN from ref. 103; (b) band structures of Mg-doped g-CN from ref. 99, Co-doped g-CN from ref. 80, Te-doped g-CN from ref. 141, La-doped g-CN from ref. 149, and Eu-doped g-CN from ref. 154.

from the valence band, which is beneficial to the transfer of photogenerated electrons.[141]

2.7 Potential characterization techniques

With the development of technology, more and more novel characterization techniques are used for the investigation of element doping. Although these techniques have not been mentioned in the literature of element-doped g-CN, they are already applied in the investigation of other materials. Herein, we will introduce some potential characterization techniques which can be used for the confirmation of doped elements in the element-doped g-CN materials.

Atom probe tomography (APT) can provide a 2D projection or 3D reconstruction of elements with great spatial resolution, which makes it suitable for the analysis of doped elements.[191] For instance, Wang's group used APT to study the details of transition-metal single atoms in a graphene shell.[189] As shown in Fig. 9(a) and (b), the 3D tomography and the projected 2D image of Ni-doped graphene shells, which reveal the distribution of C, Ni, and N atoms, are obtained through APT. To better understand the doping of Ni, the statistics of Ni atoms inside the yellow circle in Fig. 9(b) are analyzed in Fig. 9(c). Among all Ni atoms, 83% are single atoms, which means the successful doping of Ni in graphene shells.

Probe molecule FTIR spectroscopy is another potential technique that can characterize doped elements. Probe molecules, such as CO and CO_2, can be absorbed by certain microstructures, thus some characteristic FTIR bands are

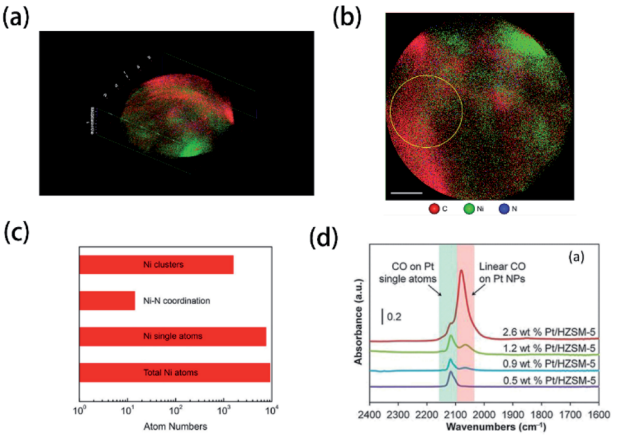

Fig. 9 (a) 3D tomography and (b) projected 2D image of Ni-doped graphene shells; (c) statistics of Ni atoms inside the yellow circle in (b). Reprinted with permission from ref. 189, copyright 2017, Elsevier. (d) FTIR spectra of CO adsorbed at saturation coverage and room temperature onto different Pt/HZSM-5 catalysts containing varying Pt weight loading. Reprinted with permission from ref. 190, copyright 2017, Elsevier.

generated.[192] In this method, characteristic FTIR bands of single atoms combined with probe molecules may be observed. Christopher's group characterized Pt-group metal based single atom catalysts *via* probe molecule FTIR spectroscopy (CO as probe molecules).[190] The FTIR spectra in Fig. 9(d) illustrate that a unique band at ~2120 cm^{-1} belongs to the absorption of CO on Pt single atoms. Therefore, probe molecule FTIR spectroscopy may be usable in the characterization of element-doped g-CN.

3. Applications of element-doped g-CN materials

In recent years, numerous novel materials involved in element-doped g-CN are investigated in-depth due to their excellent performances in various fields, such as photocatalysis, electrocatalysis, sensors, sonocatalysis, supercapacitors, and adsorbents. The effects of element-doped g-CN and the mechanisms of performance enhancement in practical applications will be discussed below.

3.1 Photocatalysis

Element-doped g-CN materials are considered as an up-and-coming metal-free photocatalyst since the early stage of related research. Up to now, the applications of photocatalysis, including the degradation of organics, hydrogen generation, and gas treatment, have been widely studied.

Most element-doped g-CN materials are efficient for the degradation of organic contaminants, such as organic dyes and antibiotics. To display the excellent performance of element-doped g-CN materials intuitively, some results of photocatalytic degradation measurements are provided in Table 3. As shown in Table 3, compared with pristine g-CN, element-doped g-CN materials have better performance for the degradation of

Table 3 Degeneration performance of element-doped g-CN for organic contaminants

Sample	Organic contaminant	Degeneration performance (according to the rate constant k, compared with pristine g-CN)	Ref.
B–P co-doped g-CN nanosheets	Oxytetracycline	2.9 times	193
Ba-doped g-CN	Tetracycline	3.25 times	147
Ce-doped g-CN	Rhodamine B	2.12 times	86
Cl-doped g-CN	Rhodamine B	4 times	164
Cu-doped g-CN	Methylene blue	2.3 times	88
Cu-doped mesoporous g-CN	Methyl orange	10.5 times	194
Fe-doped g-CN	Trimethoprim	1.33 times	195
Na-doped g-CN	Rhodamine B	3.56 times	95
P-doped g-CN	Rhodamine B	18 times	55
P-doped g-CN	Rhodamine B	2.7 times	54
P–Cl co-doped g-CN	Rhodamine B	5.9 times	103
	Antibiotic norfloxacin	2 times	
P–S co-doped g-CN	Rhodamine B	3.54 times	49
Si-doped g-CN	Rhodamine B	2.5 times	101

various organic contaminants. The effects of element-doped g-CN and the mechanisms of performance enhancement are usually revealed by various measurements. For example, the photocatalytic mechanism of P–Cl co-doped g-CN was investigated by scavenger experiments and electron spin response (ESR) experiments.[103] The results of scavenger experiments in Fig. 10(a) illustrate that the degradation ability of rhodamine B is reduced when *p*-benzoquinone (BQ, $\cdot O_2^-$ scavenger) was added into the reaction solution, which indicates that $\cdot O_2^-$ played an important role in the degradation reaction. To further confirm the effect of $\cdot O_2^-$, ESR experiments were used with 5,5-dimethyl-1-pyrroline *N*-oxide (DMPO) as a trapping agent at room temperature. As shown in Fig. 10(b), the response of $\cdot O_2^-$ species appeared under light irradiation. The above findings demonstrate that the photocatalytic activity of P–Cl co-doped g-CN is mainly attributed to $\cdot O_2^-$ species. Therefore, the photocatalytic mechanism of P–Cl co-doped g-CN can be implied as follows: the energy band structure of g-CN can also be regulated by the P–Cl co-doping and thus a stronger reducing ability to form $\cdot O_2^-$ is obtained. Photoluminescence (PL) analysis can also be used to demonstrate the mechanisms of performance enhancement. The PL spectra of pristine g-CN and Ba-doped g-CN are displayed in Fig. 10(c):[147] the lower intensity of a series of Ba-doped g-CN samples directly points out that the doping of Ba reduced the recombination of photogenerated electron–hole pairs.

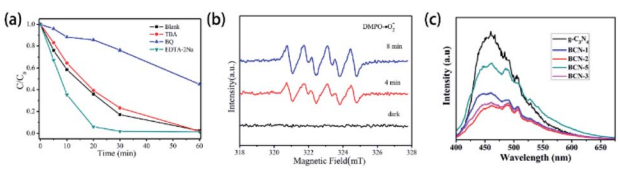

Fig. 10 (a) Species trapping experiments for the degradation of rhodamine B; (b) DMPO spin-trapping ESR spectra of P–Cl co-doped g-CN. Reprinted with permission from ref. 103, copyright 2020, Elsevier. (c) PL spectra of pristine g-CN and Ba-doped g-CN. Reprinted with permission from ref. 147, copyright 2020, Elsevier.

In addition, to cope with the increasing requirements of environmental issues, composites of element-doped g-CN and nanostructure have become a hotspot most recently. Element-doped g-CN-based composites and their excellent photocatalytic performance were reported, including Ag_2CO_3/P–S co-doped g-CN,[196] Ag_3VO_4/P–S co-doped g-CN,[198] MoS_2/S-doped g-CN,[197] S-doped rGO/S-doped g-CN,[64] carbon quantum dots supported AgI/ZnO/P-doped g-CN,[57] $Zn_3In_2S_6$/F-doped g-CN,[32] and so on. Typically, one or several kinds of nanostructures can be loaded on the element-doped g-CN matrix to obtain a composite (Fig. 11(a), (c), and (e)). Characterization of the band structures of these composites reveals that *Z*-scheme

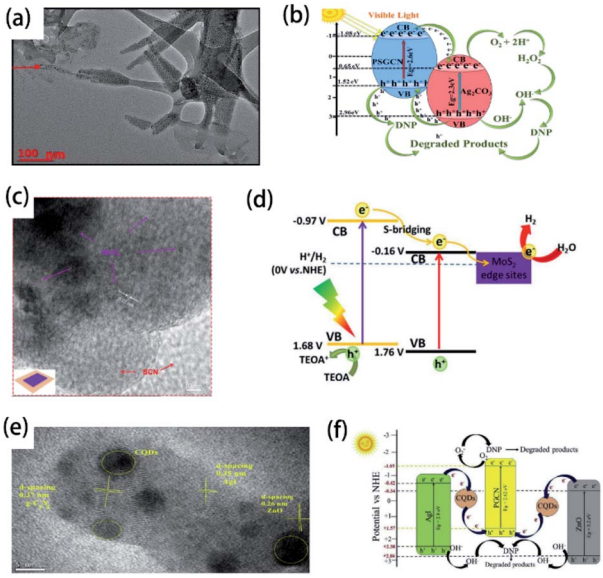

Fig. 11 (a) TEM image and (b) band structure of Ag_2CO_3/P–S co-doped g-CN. Reprinted with permission from ref. 196, copyright 2020, Elsevier. (c) TEM image and (d) band structure of MoS_2/S-doped g-CN. Reprinted with permission from ref. 197, copyright 2020, Elsevier. (e) TEM image and (f) band structure of carbon quantum dots supported AgI/ZnO/P-doped g-CN. Reprinted with permission from ref. 57, copyright 2019, Elsevier.

heterojunctions, which are conducive to the performance of photocatalysis, are formed between element-doped g-CN and the nanostructure (Fig. 11(b), (d), and (f)).

Besides the degradation of organic contaminants, photocatalysis of water splitting (including hydrogen evolution and water oxidation) is another encouraging practical application of element-doped g-CN-based materials. As shown in Fig. 12(a), B–S co-doped g-CN (CNBS),[199] (c) P-doped g-CN nanoflakes (PCNNFs),[33] (e) F-doped g-CN (GCNF),[36] (h) S-doped g-CN (MTCN),[62] (k) Co-doped g-CN (Co–g-CN),[78] and (m) Bi-doped g-CN (Bi–g-C_3N_4),[200] compared with pristine g-CN and element-doped g-CN-based materials, always possess spectacularly better H_2 evolution performance or water oxidation performance. The enhancement can be assigned to one or more of the following reasons: (1) lower recombination of photogenerated electron and hole pairs caused by the element doping according to the lower intensity in PL spectra (Fig. 12(b), (d), (i), (l), and (n)) or a stronger signal in ESR spectra (Fig. 12(f)); (2) the nitrogen adsorption–desorption isotherms (Fig. 12(g) and (j)) reveal that, in some samples, the doping process can lead to larger specific areas, which is also effective for enhancing the photocatalytic performance; (3) the dopants modify the band structure of g-CN, especially their CB positions (for H_2 evolution) or VB positions (for water oxidation), so that element-doped g-CN materials can have a better photocatalytic performance.

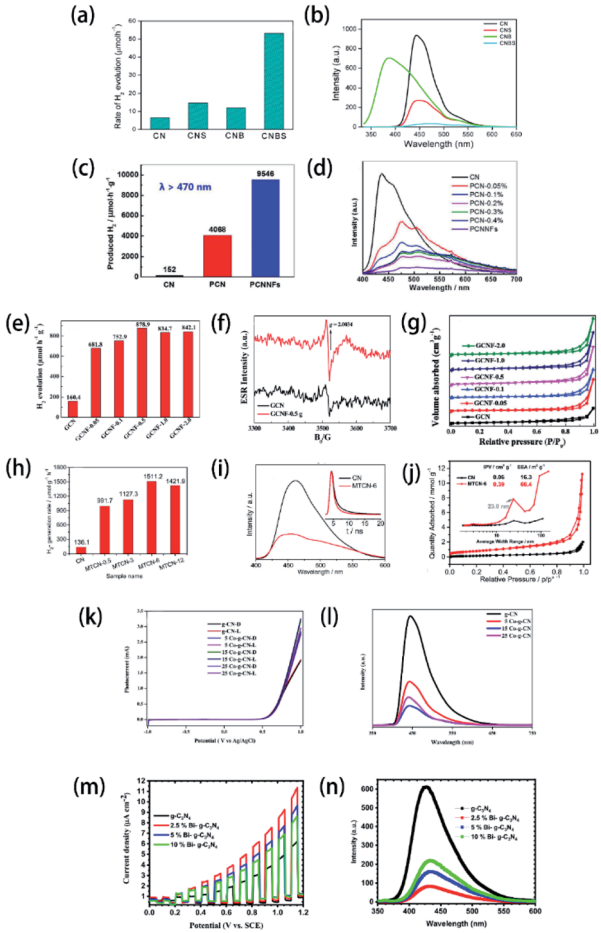

Fig. 12 (a) Photocatalytic H_2 evolution efficiency and (b) PL spectra of g-CN (CN), S-doped g-CN (CNS), B-doped g-CN (CNB), and B–S co-doped g-CN (CNBS). Reprinted with permission from ref. 199, copyright 2018, American Chemical Society. (c) Photocatalytic H_2 evolution efficiency and (d) PL spectra of g-CN (CN), P-doped g-CN (PCN), and P-doped g-CN nanoflakes (PCNNFs). Reprinted with permission from ref. 33, copyright 2018, Elsevier. (e) Photocatalytic H_2 evolution efficiency, (f) ESR spectra, and (g) N_2 adsorption–desorption isotherms of g-CN (GCN) and F-doped g-CN (GCNF). Reprinted with permission from ref. 36, copyright 2018, Royal Society of Chemistry. (h) Photocatalytic H_2 evolution efficiency, (i) PL spectra, and (j) N_2 adsorption–desorption isotherms (the inset shows the corresponding pore size distributions) of g-CN (CN) and S-doped g-CN (MTCN). Reprinted with permission from ref. 62, copyright 2018, Elsevier. (k) Linear-sweep voltammetry plots and (l) PL spectra of g-CN and Co-doped g-CN (Co-g-CN). Reprinted with permission from ref. 78, copyright 2020, Elsevier. (m) Linear-sweep voltammetry plots and (n) PL spectra of g-CN and Bi-doped g-CN (Bi-g-C_3N_4). Reprinted with permission from ref. 200, copyright 2020, Elsevier.

Under light irradiation, element-doped g-CN materials are capable of photocatalytic gas treatments. In some element-doped g-CN materials, doping can create vacancies, which are able to trap the gas molecules. Yao's group reported the photocatalytic N_2 fixation performance of I-doped g-CN, which was prepared by annealing the mixed precursor of dicyandiamide and KIO_3.[143] The introduction of I atoms produces many vacancies, which can capture photogenerated electrons (Fig. 13(a)). These electrons can reduce N_2 to form NH_4^+, which can be fixed by plants. Because of such a mechanism, the ammonia evolution rate of I-doped g-CN reaches 200.8 mg L^{-1} g_{cat}^{-1}, which is 2.8 times higher than that of pristine g-CN. For other element-doped g-CN materials, dopants can promote the separation of photogenerated electrons and holes and thereby catalyze the gas reactions. Such a mechanism (Fig. 13(b)) can demonstrate the NO_x removal by B-doped g-CN nanotubes (their NO removal rate is 1.5 times higher than that of pristine g-

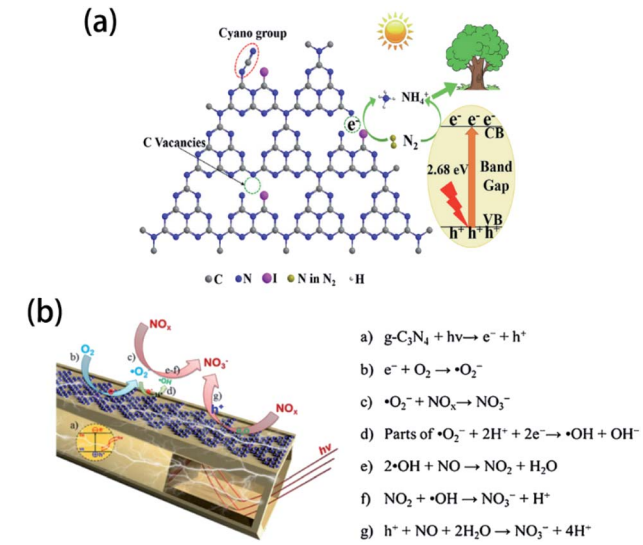

Fig. 13 (a) Mechanism of N_2 fixation on I-doped g-CN. Reprinted with permission from ref. 143, copyright 2020, Elsevier. (b) Mechanism of NO_x reduction on B-doped g-CN nanotubes. Reprinted with permission from ref. 48, copyright 2018, Elsevier.

Table 4 Tafel slope values of some element-doped g-CN materials

Sample	Reaction type	Tafel slope of sample (mV dec^{-1})	Tafel slope of reference (mV dec^{-1})	Ref.
S-doped g-CN	HER	196	238 (g-CN)	135
Mo-doped g-CN	HER	180	238 (g-CN)	135
Mo–S co-doped g-CN	HER	110	238 (g-CN)	135
RhP@P-doped g-CN	HER	38.4	38.1 (Pt/C)	58
Cu-doped g-CN	HER	76	164 (g-CN)	119
S-doped g-CN/RGO	OER	115	158 (RGO)	84
Fe-doped g-CN	ORR	73	84.5 (g-CN) 76.5 (Pt/C)	174

CN)[48] and the reduction of CO_2 by P-doped g-CN nanotubes (their CO_2 reduction rate is 13.92 times higher than that of pristine g-CN).[201]

3.2 Electrocatalysis

It is well known that semiconductors are capable of electrocatalysis, including the oxygen reduction reaction (ORR), hydrogen evolution reaction (HER), and oxygen evolution reaction (OER), so element-doped g-CN-based materials have great potential as candidates for electrocatalysts. Typically, element-doped g-CN can provide many active sites, leading to the catalysis effect for electrochemical reactions on electrodes. To show the excellent performance of element-doped g-CN materials directly, some results of electrocatalytic measurements are provided in Table 4.

Many efforts have been devoted to electrocatalysis for ORR, which is one of the promising applications of element-doped g-CN. For example, Dey's group reported transition-metal-doped g-CN for highly efficient ORR.[174] Tafel plots of Fe-g-CN, g-CN, and commercial Pt/C are shown in Fig. 14(a); it is obvious from the figure that the Tafel slope of Fe-g-CN (73 mV dec^{-1}) is much smaller than those of g-CN (84.5 mV dec^{-1}) and commercial Pt/C (76.5 mV dec^{-1}), which suggests the better electrocatalytic activity of Fe-g-CN. Its enhanced performance results from the absorption of O_2 on Fe–N_x active sites of Fe-doped g-CN, which in turn promotes the process of ORR (the mechanism is shown in Fig. 14(b)). To further improve the electrocatalytic performance, the preparation of element-doped g-CN-contained composites is considered a useful strategy. Zhou's group prepared the composite of Co-doped g-CN and ordered mesoporous carbon (Co–C_3N_4/OMC) as the electrocatalyst for ORR.[77] The Tafel slopes in Fig. 14(c) show that the electrocatalytic activity of Co–C_3N_4/OMC (84 mV dec^{-1}) is significantly higher than that of Co–C_3N_4 (189 mV dec^{-1}), which implies that the conductivity of OMC plays a crucial role in the improvement of electrocatalytic performance.

Electrocatalysis for water splitting is also an important application of element-doped g-CN due to the demand for sustainable energy. Generally, electrochemical water splitting consists of two electrode half-reactions: HER at the cathode and OER at the anode; and element-doped g-CN can serve as the electrocatalyst for the above two reactions. Tonda's group prepared Co-coordinated S-doped g-CN on reduced graphene oxide (RGO) as an efficient bifunctional electrocatalyst for water splitting.[84] The Tafel plots of various samples for HER and OER are shown in Fig. 14(d) and (e), respectively. As is seen from the Tafel slopes, the optimized Co–C_3N_4/OMC shows a better electrocatalytic performance than RGO and SCN/RGO in both HER and OER due to the conductivity of RGO and the active sites provided by Co–(N, S)–C.

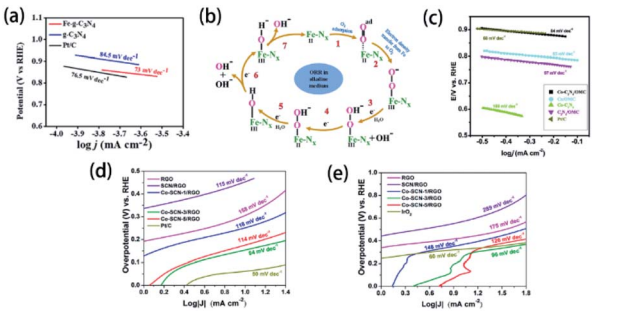

Fig. 14 (a) Tafel plots of the Fe-g-CN, g-CN, and Pt/C catalysts and (b) ORR mechanism of the Fe–N_x active sites of Fe-g-CN. Reprinted with permission from ref. 174, copyright 2020, American Chemical Society. (c) Tafel plots of Co–C_3N_4, C_3N_4/OMC, Pt/C, Co–C_3N_4/OMC-2, and Co/OMC. Reprinted with permission from ref. 77, copyright 2019, Elsevier. Tafel plots of RGO, SCN/RGO, Co–SCN-1/RGO, Co–SCN-3/RGO, Co–SCN-5/RGO, and Pt/C catalysts for (d) HER and (e) OER, respectively. Reprinted with permission from ref. 84, copyright 2019, American Chemical Society.

3.3 Sensors

Element-doped g-CN can be used to detect certain substances due to its unique structure and properties. Therefore, element-doped g-CN-contained materials are fascinating choices for sensitive and selective sensors.

Organics in the solution can be involved in the electrochemical process on electrodes. The electrochemical reactions of organics lead to the current response, and the current density is closely related to the concentration of organics. Based on this phenomenon, an electrochemical sensor can be achieved to detect organics. Additionally, element-doped g-CN-contained materials modified electrodes can largely enhance the current density in the presence of a small concentration of organics. For example, Mohammad's group prepared S-doped g-CN modified fluorine-doped tin oxide (S-g-C_3N_4/FTO) for electrochemical

sensing of hydrazine (the mechanism diagram is shown in Fig. 15(a)).[202] Linear-sweep voltammetry (LSV) measurements reveal that the S-g-C_3N_4/FTO/hydrazine system has much higher current density than other systems (Fig. 15(b)), and its current density changes with the concentrations of hydrazine (Fig. 15(c)), which show a detection limit as low as 0.06 μM with a linear range of 60–475 mM. The above results determine the feasibility of the S-g-CN/FTO sensor for hydrazine detection. Similar methods can be used to detect other organics, such as acetaminophen,[204] nitrofurantoin,[173] metronidazole,[205] and 4-nitrophenol.[61]

Besides current density, electrochemiluminescence (ECL) intensity can be a characteristic response too. Li's group reported a sensor system including S-doped g-CN nanosheets for the detection of folic acid according to the ECL behavior (the mechanism diagram is shown in Fig. 15(d)).[203] It was found that the ECL signal decreased gradually with the addition of folic acid to the S-doped g-CN nanosheet/N-doped carbon dot system (Fig. 15(e)). Therefore, a novel sensor for detecting folic acid, whose detection limit is 16 nM with a linear range of 0.05–200 μM, was successfully prepared. The sensing of other organics, such as L-cysteine,[206] and K-RAS gene,[169] can be achieved *via* ECL measurements.

Element-doped g-CN-based sensor systems are also useful to detect heavy metal ions, which are ubiquitous in environmental pollutants. In some sensor systems, doped elements can play a crucial role in detecting ions. According to Jiang's group, the high-sensitive, selective, repeatable, and stable electrochemical sensor of S-doped g-CN nanoflakes modified glassy carbon electrode (S-g-CN–GCE) is able to detect Pb^{2+} ions.[207] Based on the strong interaction between the doped S atoms and Pb^{2+} ions, S-g-CN–GCE can detect Pb^{2+} ions *via* differential pulse voltammetry (DPV) measurements, which exhibited a detection limit of 3.0×10^{-9} mol L^{-1} within the Pb^{2+} concentration range of 7.5×10^{-8} to 2.5×10^{-6} mol L^{-1} and 2.5×10^{-6} to 1×10^{-3} mol L^{-1}. Moreover, fixing metal nanoparticles on element-doped g-CN is another feasible method to detect ions. Ramaraj's group has reported a new system of chitosan functionalized Au nanoparticles assembled S-doped g-CN as the sensitive and selective detector of trace Hg^{2+} ions due to the interaction between Au nanoparticles and Hg^{2+}, and this system possessed a lower limit of detection of 0.275 nM than other systems.[168]

Furthermore, based on detection requirements, many more techniques can be applied for sensors, such as the chemiluminescent platform applied for the sensing of H_2S in the human plasma by efficient Cu^{2+} modified g-CN nanosheets enhanced luminol–H_2O_2 system,[120] and UV-vis absorption spectra for the detection of glucose by Fe-doped g-CN nanoparticles.[68]

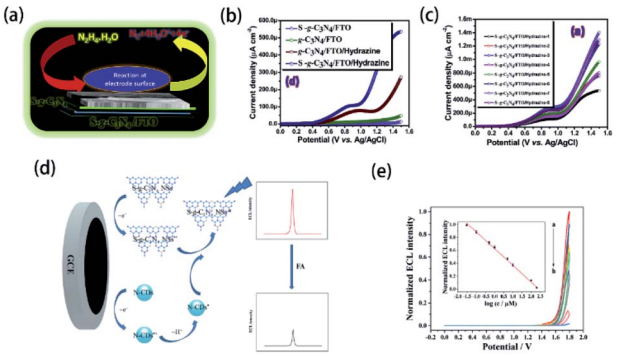

Fig. 15 (a) Mechanism diagram of the S-g-CN/FTO sensor for hydrazine, (b) LSV measurements for S-g-CN/FTO, g-CN/FTO, g-CN/FTO/hydrazine, and S-g-CN/FTO/hydrazine, and (c) LSV measurements at varying concentrations of hydrazine. Reprinted with permission from ref. 202, copyright 2020, Elsevier. (d) Mechanism diagram of S-doped g-CN nanosheets/nitrogen-doped carbon dot system and (e) the ECL response of folic acid at (a) 0.05 μM, (b) 0.1 μM, (c) 0.5 μM, (d) 1 μM, (e) 5 μM, (f) 10 μM, (g) 100 μM, and (h) 200 μM concentrations (the inset shows a linear calibration plot for folic acid). Reprinted with permission from ref. 203, copyright 2019, Springer.

3.4 Sonocatalysis

Recently, sonodegradation has attracted great attention in the field of wastewater treatment. In wastewater, with the breaking of bubbles under ultrasonic treatment, extreme pressure and temperature are generated around the bubbles, which is positive for the oxidation of organic pollutants.[208,209] As a result, sonocatalysis, a state-of-the-art technique, is considered a promising way to solve environmental problems.

Element-doped g-CN-based materials are promising candidates for sonocatalysts. Yang's group prepared the composite of S-doped g-CN and $CoFe_2O_4$ (SCN/$CoFe_2O_4$) *via* the calcination of H_2SO_4-treated dicyandiamide, followed by the reaction of $Co(NO_3)_2 \cdot 6H_2O$, $Fe(NO_3)_3 \cdot 9H_2O$ and NaOH in a SCN-dispersed solution.[210] The samples were applied to degrade methylene blue, and the sonocatalytic results of various systems are shown in Fig. 16(a). The SCN/$CoFe_2O_4$/H_2O_2/US system exhibited the highest degradation performance of 96% in 20 min. Additionally, the pseudo-first-order kinetic constant of the SCN/$CoFe_2O_4$/H_2O_2/US system is 4.84 times higher than that of the $CoFe_2O_4$/H_2O_2/US system, which suggested the positive effect of SCN. Remarkably, the degradation performances of rhodamine B and Congo red were lower than that of methylene blue (Fig. 16(b)), indicating that the performance can be influenced by the dye sizes, structural compositions, and electric charges. Therefore, the modification and mechanism of sonocatalysts should be investigated further.

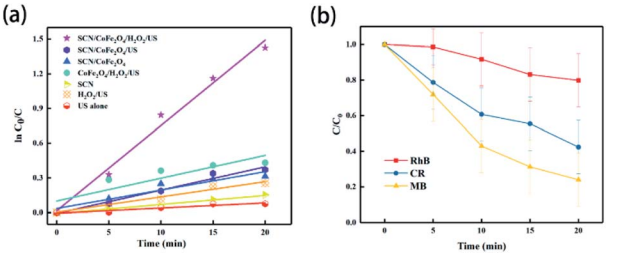

Fig. 16 (a) Plot of ln(C_0/C) *vs.* ultrasonication time in the sonocatalysis measurements of various systems for methylene blue (US: ultrasonication); (b) effect of different type of organic dye on sonodegradation (RhB: rhodamine B, CR: Congo red, and MB: methylene blue). Reprinted with permission from ref. 210, copyright 2020, MDPI.

3.5 Supercapacitors

Inspired by the application of two-dimensional graphitic carbon materials as supercapacitors due to their unique electronic properties, Shen's group reported the utility of porous B-doped g-CN nanosheet electrodes as supercapacitors.[45] Electrochemical measurements exhibited that porous B-doped g-CN nanosheets had a better capacitive performance than g-CN: the cyclic voltammetry (CV) results of porous B-doped g-CN nanosheets and g-CN in Fig. 17(a) show that the enclosed area of the CV curve of porous B-doped g-CN nanosheets is much larger than that of g-CN, suggesting the better capacitive performance of the former; and the calculated results of their specific capacitances at different current densities in Fig. 17(b) show that porous B-doped g-CN nanosheets have a higher capacitance than that of g-CN; the results of repeated charge–discharge measurement in Fig. 17(c) show that the specific capacitance of porous B-doped g-CN nanosheets is stable after 2500 cycles. The above results demonstrate the high electrochemical capacitive properties of porous B-doped g-CN nanosheets. Moreover, a further study of Shen's group modified the B-doped g-CN material and thus enhanced its specific capacitance (~660.6 F g^{-1}), which is 3.02 times higher than that of pristine g-CN (~218.7 F g^{-1}) and have exceeded most of the reported carbon electrode materials.[46] So, this work may boost the development of high-performance supercapacitor materials.

3.6 Adsorbents

Generally, there are some hazardous heavy metal ions in industrial wastewater. As a result, various adsorption materials have been developed to remove these ions due to the interaction between the functional groups and ions.[211–213] Element-doped g-CN, as a kind of functionalized porous material, possesses promising adsorption performance to ions. Wang's group provided an ideal tool for mercury (Hg^{2+}) removal *via* S-doped g-CN nanotubes/graphene oxide aerogel (SGA) adsorbent.[177] As shown in Fig. 18(a), under certain conditions (pH = 5, 25 °C, [SGA] = 1.0 g L^{-1}, [Hg^{2+}] = 50 mg L^{-1}, and 120 min), the removal efficiency of SGA towards Hg^{2+} initially and after four cycles are 83.3% and 58.1%, respectively, which suggests that this adsorbent has great potential in ion removal. The investigation of the adsorption mechanism reveals that the excellent performance can be attributed to the specific binding of S atoms to Hg^{2+} (Fig. 18(b)) and the high mobility of Hg^{2+} in S-doped g-CN nanotubes (Fig. 18(c)).

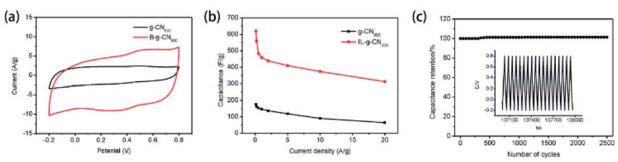

Fig. 17 (a) CV curves of B-doped g-CN nanosheets and g-CN; (b) specific capacitances of B-doped g-CN nanosheets and g-CN at different current densities; (c) repeated charge–discharge measurement of B-doped g-CN nanosheets. Reprinted with permission from ref. 45, copyright 2017, Elsevier.

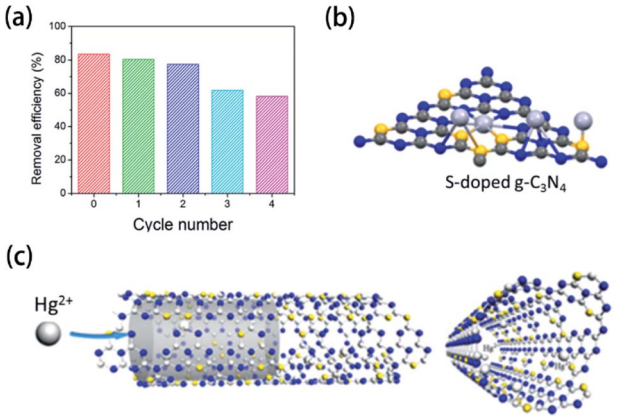

Fig. 18 (a) Removal efficiency of Hg^{2+} by SGA at different regeneration cycles; (b) specific binding of S atoms to Hg^{2+}; and (c) mobility of Hg^{2+} in S-doped g-CN nanotubes. Reprinted with permission from ref. 177, copyright 2020, Elsevier.

4. Conclusions

Herein, we have highlighted the significant characterization techniques for the determination of heteroatoms in element-doped g-CN. Typically, XPS, which can certify the presence of the doped elements in the microstructure of g-CN, is the most frequently used method in the characterization of element-doped g-CN. To achieve a better understanding of the doped elements, more details can be obtained by NMR, FTIR spectroscopy, XAS, elemental mapping, and EELS. Moreover, some advanced characterization techniques, such as APT and probe molecule FTIR spectroscopy, offer exciting opportunities for the characterization of doped elements in g-CN.

With the study of element doping in g-CN, the application fields of g-CN-based materials are increasingly enlarged. Conventionally, g-CN-based materials, including element-doped g-CN, are ideal choices for photocatalysts. Therefore, the vast majority of research results of element-doped g-CN have been focused on photocatalysis in recent years. Meanwhile, these materials are also expected to have potential applications in other applications, such as electrocatalysis, sensors, sonocatalysis, supercapacitors, and adsorbents.

Overall, the characterization of element-doped g-CN and related materials is a significant work, as well as a huge challenge. The excellent properties of these materials are a great impetus to research efforts to explore practical applications. Last but not least, we hope that the information provided in this review can play a role in the future research of element-doped g-CN-based materials.

Conflicts of interest

There are no conflicts to declare.

Acknowledgements

The authors are grateful for the financial support from the National Key Research and Development Program of China

(2017YFA0207301) and the National Natural Science Foundation of China (21890751, 21471036).

Notes and references

1 X. Zhang, X. Yuan, L. Jiang, J. Zhang, H. Yu, W. Hou and G. Zeng, *Chem. Eng. J.*, 2020, **390**, 124475.
2 I. Som, M. Roy and R. Saha, *ChemCatChem*, 2020, **12**, 3409–3433.
3 T. Su, Z. Qin, H. Ji and Z. Wu, *Nanotechnology*, 2019, **30**, 502002.
4 S. Y. Lim, C. S. Law, L. Liu, M. Markovic, C. Hedrich, R. H. Blick, A. D. Abell, R. Zierold and A. Santos, *Catalysts*, 2019, **9**, 988.
5 I. J. Ani, U. G. Akpan, M. A. Olutoye and B. H. Hameed, *J. Clean. Prod.*, 2018, **205**, 930–954.
6 H. Abdullah, M. M. R. Khan, H. Ong and Z. Yaakob, *J. CO_2 Util.*, 2017, **22**, 15–32.
7 R. Asahi, T. Morikawa, T. Ohwaki, K. Aoki and Y. Taga, *Science*, 2001, **293**, 269–271.
8 Y. Cheng, R. Song, K. Wu, N. Peng, M. Yang, J. Luo, T. Zou, Y. Zuo and Y. Liu, *J. Hazard. Mater.*, 2020, **383**, 121166.
9 J. Wang, D. Liu, Y. Zhu, S. Zhou and S. Guan, *Appl. Catal., B*, 2018, **231**, 251–261.
10 X. Wang, K. Maeda, A. Thomas, K. Takanabe, G. Xin, J. M. Carlsson, K. Domen and M. Antonietti, *Nat. Mater.*, 2009, **8**, 76–80.
11 I. F. Teixeira, E. C. M. Barbosa, S. C. E. Tsang and P. H. C. Camargo, *Chem. Soc. Rev.*, 2018, **47**, 7783–7817.
12 H. Wang, M. Li, H. Li, Q. Lu, Y. Zhang and S. Yao, *Mater. Des.*, 2019, **162**, 210–218.
13 S. Cao, J. Low, J. Yu and M. Jaroniec, *Adv. Mater.*, 2015, **27**, 2150–2176.
14 Y. Zhang, J. Liu, G. Wu and W. Chen, *Nanoscale*, 2012, **4**, 5300–5303.
15 C. Liu, Y. Zhang, F. Dong, X. Du and H. Huang, *J. Phys. Chem. C*, 2016, **120**, 10381–10389.
16 H. Fan, N. Wang, Y. Tian, S. Ai and J. Zhan, *Carbon*, 2016, **107**, 747–753.
17 W. Ong, L. Tan, Y. Ng, S. Yong and S. Chai, *Chem. Rev.*, 2016, **116**, 7159–7329.
18 J. Zhou, J. Xue, Q. Pan, X. Yang, Q. Shen, T. Ma, X. Liu and H. Jia, *J. Photochem. Photobiol., A*, 2019, **372**, 147–155.
19 S. Zhang, C. Hu, H. Ji, L. Zhang and F. Li, *Appl. Surf. Sci.*, 2019, **478**, 304–312.
20 E. Murugan, S. Santhosh Kumar, K. M. Reshna and S. Govindaraju, *J. Mater. Sci.*, 2018, **54**, 5294–5310.
21 T. Arumugham, R. G. Amimodu, N. J. Kaleekkal and D. Rana, *J. Environ. Sci.*, 2019, **82**, 57–69.
22 X. Zhang, L. Li, Y. Zeng, F. Liu, J. Yuan, X. Li, Y. Yu, X. Zhu, Z. Xiong, H. Yu and Y. Xie, *ACS Appl. Nano Mater.*, 2019, **2**, 7255–7265.
23 H. Yu, R. Shi, Y. Zhao, T. Bian, Y. Zhao, C. Zhou, G. I. N. Waterhouse, L. Wu, C. Tung and T. Zhang, *Adv. Mater.*, 2017, **29**, 1605148.
24 M. Yousefi, S. Villar-Rodil, J. I. Paredes and A. Z. Moshfegh, *J. Alloys Compd.*, 2019, **809**, 151783.
25 G. Lei, Y. Cao, W. Zhao, Z. Dai, L. Shen, Y. Xiao and L. Jiang, *ACS Sustainable Chem. Eng.*, 2019, **7**, 4941–4950.
26 D. K. Chauhan, S. Jain, V. R. Battula and K. Kailasam, *Carbon*, 2019, **152**, 40–58.
27 M. Inagaki, T. Tsumura, T. Kinumoto and M. Toyoda, *Carbon*, 2019, **141**, 580–607.
28 C. Xu, W. Zhang, K. Deguchi, S. Ohki, T. Shimizu, R. Ma and T. Sasaki, *J. Mater. Chem. A*, 2020, **8**, 13299–13310.
29 N. Zhang, C. Chen, Y. Chen, G. Chen, C. Liao, B. Liang, J. Zhang, A. Li, B. Yang, Z. Zheng, X. Liu, A. Pan, S. Liang and R. Ma, *ACS Appl. Energy Mater.*, 2018, **1**, 2016–2023.
30 X. Wang, X. Chen, A. Thomas, X. Fu and M. Antonietti, *Adv. Mater.*, 2009, **21**, 1609–1612.
31 Y. Wang, Y. Di, M. Antonietti, H. Li, X. Chen and X. Wang, *Chem. Mater.*, 2010, **22**, 5119–5121.
32 Y. Wu, H. Wang, W. Tu, Y. Liu, S. Wu, Y. Tan and J. Chew, *Appl. Catal., B*, 2018, **233**, 58–69.
33 H. Fang, X. Zhang, J. Wu, N. Li, Y. Zheng and X. Tao, *Appl. Catal., B*, 2018, **225**, 397–405.
34 I. Palchan, M. Crespin, H. Estradeszwarckopf and B. Rousseau, *Chem. Phys. Lett.*, 1989, **157**, 321–327.
35 D. Gao, Y. Liu, M. Song, S. Shi, M. Si and D. Xue, *J. Mater. Chem. C*, 2015, **3**, 12230–12235.
36 Y. Liu, J. Wang, C. Yin, H. Duan, S. Kang and L. Cui, *RSC Adv.*, 2018, **8**, 27021–27026.
37 A. Mirzaei, Z. Chen, F. Haghighat and L. Yerushalmi, *Appl. Catal., B*, 2019, **242**, 337–348.
38 X. Guo, L. Rao, P. Wang, L. Zhang and Y. Wang, *Int. J. Environ. Res. Publ. Health*, 2019, **16**, 581.
39 S. Yan, Z. Li and Z. Zou, *Langmuir*, 2010, **26**, 3894–3901.
40 Y. Wang, H. Li, J. Yao, X. Wang and M. Antonietti, *Chem. Sci.*, 2011, **2**, 446–450.
41 Q. Gu, J. Liu, Z. Gao and C. Xue, *Chem. - Asian J.*, 2016, **11**, 3169–3173.
42 S. Thaweesak, S. Wang, M. Lyu, M. Xiao, P. Peerakiatkhajohn and L. Wang, *Dalton Trans.*, 2017, **46**, 10714–10720.
43 J. Zhu, T. Diao, W. Wang, X. Xu, X. Sun, S. A. C. Carabineiro and Z. Zhao, *Appl. Catal., B*, 2017, **219**, 92–100.
44 Y. Shiraishi, K. Chishiro, S. Tanaka and T. Hirai, *Langmuir*, 2020, **36**, 734–741.
45 L. Kong, Q. Chen, X. Shen, C. Xia, Z. Ji and J. Zhu, *Electrochim. Acta*, 2017, **245**, 249–258.
46 L. Kong, Q. Chen, X. Shen, G. Zhu and J. Zhu, *J. Colloid Interface Sci.*, 2018, **532**, 261–271.
47 J. Zhao, Y. Liu, Y. Wang, H. Li, J. Wang and Z. Li, *Appl. Surf. Sci.*, 2019, **470**, 923–932.
48 Z. Wang, M. Chen, Y. Huang, X. Shi, Y. Zhang, T. Huang, J. Cao, W. Ho and S. Lee, *Appl. Catal., B*, 2018, **239**, 352–361.
49 J. Li, Y. Qi, Y. Mei, S. Ma, Q. Li, B. Xin, T. Yao and J. Wu, *J. Colloid Interface Sci.*, 2020, **566**, 495–504.
50 Y. Zhang, T. Mori, J. Ye and M. Antonietti, *J. Am. Chem. Soc.*, 2010, **132**, 6294–6295.
51 T. Ma, J. Ran, S. Dai, M. Jaroniec and S. Qiao, *Angew. Chem., Int. Ed.*, 2015, **54**, 4646–4650.
52 J. Su, P. Geng, X. Li, Q. Zhao, X. Quan and G. Chen, *Nanoscale*, 2015, **7**, 16282–16289.

53 S. Guo, Z. Deng, M. Li, B. Jiang, C. Tian, Q. Pan and H. Fu, *Angew. Chem., Int. Ed.*, 2016, **55**, 1830–1834.
54 B. Chai, J. Yan, C. Wang, Z. Ren and Y. Zhu, *Appl. Surf. Sci.*, 2017, **391**, 376–383.
55 P. Wang, C. Guo, S. Hou, X. Zhao, L. Wu, Y. Pei, Y. Zhang, J. Gao and J. Xu, *J. Alloys Compd.*, 2018, **769**, 503–511.
56 X. Wang, X. Li, W. Chen, R. Wang, W. Bian and M. M. F. Choi, *Spectrochim. Acta, Part A*, 2018, **198**, 1–6.
57 V. Hasija, A. Sudhaik, P. Raizada, A. Hosseini-Bandegharaei and P. Singh, *J. Environ. Chem. Eng.*, 2019, **7**, 103272.
58 C. Xu, Q. Wang, R. Ding, Y. Wang, Y. Zhang and G. Fan, *Appl. Surf. Sci.*, 2019, **489**, 796–801.
59 S. Cao, Q. Huang, B. Zhu and J. Yu, *J. Power Sources*, 2017, **351**, 151–159.
60 G. Liu, P. Niu, C. Sun, S. C. Smith, Z. Chen, G. Lu and H. Cheng, *J. Am. Chem. Soc.*, 2010, **132**, 11642–11648.
61 C. Rajkumar, P. Veerakumar, S. M. Chen, B. Thirumalraj and K. C. Lin, *ACS Sustainable Chem. Eng.*, 2018, **6**, 16021–16031.
62 H. Wang, Y. Bian, J. Hu and L. Dai, *Appl. Catal., B*, 2018, **238**, 592–598.
63 W. Cha, I. Y. Kim, J. M. Lee, S. Kim, K. Ramadass, K. Gopalakrishnan, S. Premkumar, S. Umapathy and A. Vinu, *ACS Appl. Mater. Interfaces*, 2019, **11**, 27192–27199.
64 S. Joseph, S. Abraham, T. Abraham, R. N. Priyanka and B. Mathew, *Appl. Surf. Sci.*, 2019, **495**, 143478.
65 Z. Li, G. Gu, S. Hu, X. Zou and G. Wu, *Chin. J. Catal.*, 2019, **40**, 1178–1186.
66 H. Qin, W. Lv, J. Bai, Y. Zhou, Y. Wen, Q. He, J. Tang, L. Wang and Q. Zhou, *J. Mater. Sci.*, 2018, **54**, 4811–4820.
67 W. Miao, Y. Liu, X. Chen, Y. Zhao and S. Mao, *Carbon*, 2020, **159**, 461–470.
68 J. Xian, Y. Weng, H. Guo, Y. Li, B. Yao and W. Weng, *Spectrochim. Acta, Part A*, 2019, **215**, 218–224.
69 H. Li, C. Shan and B. Pan, *Sci. Total Environ.*, 2019, **675**, 62–72.
70 J. Zhu, S. A. C. Carabineiro, D. Shan, J. L. Faria, Y. Zhu and J. L. Figueiredo, *J. Catal.*, 2010, **274**, 207–214.
71 S. Tonda, S. Kumar, S. Kandula and V. Shanker, *J. Mater. Chem. A*, 2014, **2**, 6772–6780.
72 W. Luo, W. Huang, X. Feng, Y. Huang, X. Song, H. Lin, S. Wang and G. Mailhot, *RSC Adv.*, 2020, **10**, 21876–21886.
73 T. Ma, Q. Shen, B. Zhao, J. Xue, R. Guan, X. Liu, H. Jia and B. Xu, *Inorg. Chem. Commun.*, 2019, **107**, 107451.
74 J. Hu, P. Zhang, W. An, L. Liu, Y. Liang and W. Cui, *Appl. Catal., B*, 2019, **245**, 130–142.
75 X. Yang, X. Cao, B. Tang, B. Shan, M. Deng and Y. Liu, *J. Photochem. Photobiol., A*, 2019, **375**, 40–47.
76 Z. Ding, X. Chen, M. Antonietti and X. Wang, *ChemSusChem*, 2011, **4**, 274–281.
77 M. Hassan, T. Liu, X. Bo and M. Zhou, *J. Phys. Chem. Solids*, 2019, **131**, 111–118.
78 B. Babu, J. Shim and K. Yoo, *Ceram. Int.*, 2020, **46**, 16422–16430.
79 X. Cao, X. Chi, X. Deng, Q. Sun, X. Gong, B. Yu, A. C. Y. Yuen, W. Wu and R. K. Y. Li, *Polymers*, 2020, **12**, 1106.
80 Z. Zhu, X. Tang, W. Fan, Z. Liu, P. Huo, T. Wang, Y. Yan and C. Li, *J. Alloys Compd.*, 2019, **775**, 248–258.
81 Z. Honda, M. Saito, F. Takenaka, N. Kamata, Y. Sawada, T. Kida and M. Hagiwara, *Solid State Sci.*, 2019, **98**, 106017.
82 J. Fan, H. Qin and S. Jiang, *Chem. Eng. J.*, 2019, **359**, 723–732.
83 X. Xu, S. Wang, T. Hu, X. Yu, J. Wang and C. Jia, *Dyes Pigments*, 2020, **175**, 108107.
84 W. K. Jo, S. Moru and S. Tonda, *ACS Sustainable Chem. Eng.*, 2019, **7**, 15373–15384.
85 C. Wu, X. Zhang, Z. Xia, M. Shu, H. Li, X. Xu, R. Si, A. I. Rykov, J. Wang, S. Yu, S. Wang and G. Sun, *J. Mater. Chem. A*, 2019, **7**, 14001–14010.
86 R. Jin, S. Hu, J. Gui and D. Liu, *Bull. Korean Chem. Soc.*, 2015, **36**, 17–23.
87 Y. Yang, M. Guo, G. Zhang and W. Li, *Carbon*, 2017, **117**, 120–125.
88 H. Dou, L. Chen, S. Zheng, Y. Zhang and G. Xu, *Mater. Chem. Phys.*, 2018, **214**, 482–488.
89 T. Choudhury, S. O. Saied, J. L. Sullivan and A. M. Abbot, *J. Phys. D: Appl. Phys.*, 1989, **22**, 1185–1195.
90 D. P. Ojha, H. P. Karki, J. H. Song and H. J. Kim, *Composites, Part B*, 2019, **160**, 277–284.
91 X. Chen, J. Zhang, X. Fu, M. Antonietti and X. Wang, *J. Am. Chem. Soc.*, 2009, **131**, 11658–11659.
92 Y. Chen, X. Liu, L. Hou, X. Guo, R. Fu and J. Sun, *Chem. Eng. J.*, 2020, **383**, 123132.
93 C. Zhang, M. Zhang, Y. Li and D. Shuai, *Appl. Catal., B*, 2019, **248**, 11–21.
94 L. K. Putri, B. J. Ng, W. J. Ong, H. W. Lee, W. S. Chang and S. P. Chai, *J. Mater. Chem. A*, 2018, **6**, 3181–3194.
95 J. Zhang, S. Hu and Y. Wang, *RSC Adv.*, 2014, **4**, 62912–62919.
96 L. Zhang, N. Ding, M. Hashimoto, K. Iwasaki, N. Chikamori, K. Nakata, Y. Xu, J. Shi, H. Wu, Y. Luo, D. Li, A. Fujishima and Q. Meng, *Nano Res.*, 2018, **11**, 2295–2309.
97 Y. Shang, Y. Ma, X. Chen, X. Xiong and J. Pan, *Mol. Catal.*, 2017, **433**, 128–135.
98 Z. Shu, Y. Wang, W. Wang, J. Zhou, T. Li, X. Liu, Y. Tan and Z. Zhao, *Int. J. Hydrogen Energy*, 2019, **44**, 748–756.
99 S. B. Vuggili, S. K. Khanth, K. Kadiya, U. K. Gaur and M. Sharma, *J. Environ. Chem. Eng.*, 2019, **7**, 103440.
100 M. M. Islam, R. D. Tentu, M. A. Ali and S. Basu, *ChemistrySelect*, 2018, **3**, 11241–11250.
101 Z. Liang, G. Ba, H. Li, N. Du and W. Hou, *J. Alloys Compd.*, 2020, **815**, 152488.
102 C. Li, S. Yu, X. Zhang, Y. Wang, C. Liu, G. Chen and H. Dong, *J. Colloid Interface Sci.*, 2019, **538**, 462–473.
103 Y. Yang, H. Jin, C. Zhang, H. Gan, F. Yi and H. Wang, *J. Alloys Compd.*, 2020, **821**, 153439.
104 M. Zhang, X. Bai, D. Liu, J. Wang and Y. Zhu, *Appl. Catal., B*, 2015, **164**, 77–81.
105 S. Hu, F. Li, Z. Fan, F. Wang, Y. Zhao and Z. Lv, *Dalton Trans.*, 2015, **44**, 1084–1092.
106 M. Wu, J. Yan, X. Tang, M. Zhao and Q. Jiang, *ChemSusChem*, 2014, **7**, 2654–2658.
107 Y. Guo, Q. Liu, Z. Li, Z. Zhang and X. Fang, *Appl. Catal., B*, 2018, **221**, 362–370.
108 X. Wu, D. Long, X. Rao and Y. Zhang, *J. Photochem. Photobiol., A*, 2020, **401**, 112759.
109 L. Chen, D. Zhu, J. Li, X. Wang, J. Zhu, P. S. Francis and Y. Zheng, *Appl. Catal., B*, 2020, **273**, 9.

110 S. Wang, J. Zhan, K. Chen, A. Ali, L. Zeng, H. Zhao, W. Hu, L. Zhu and X. Xu, *ACS Sustainable Chem. Eng.*, 2020, **8**, 8214–8222.
111 R. Zhang, S. Niu, X. Zhang, Z. Jiang, J. Zheng and C. Guo, *Appl. Surf. Sci.*, 2019, **489**, 427–434.
112 I. N. Reddy, L. V. Reddy, N. Jayashree, C. V. Reddy, M. Cho, D. Kim and J. Shim, *Chemosphere*, 2021, **264**, 128593.
113 T. Cao, M. Cai, L. Jin, X. Wang, J. Yu, Y. Chen and L. Dai, *New J. Chem.*, 2019, **43**, 16169–16175.
114 G. Lei, W. Zhao, L. Shen, S. Liang, C. Au and L. Jiang, *Appl. Catal., B*, 2020, **267**, 12.
115 Q. Chen, H. Dou, S. Zheng, X. Rao and Y. Zhang, *J. Photochem. Photobiol., A*, 2019, **382**, 111931.
116 P. Deng, J. Xiong, S. Lei, W. Wang, X. Ou, Y. Xu, Y. Xiao and B. Cheng, *J. Mater. Chem. A*, 2019, **7**, 22385–22397.
117 L. Li, M. Liang, J. Huang, S. Zhang, Y. Liu and F. Li, *Environ. Sci. Pollut. Res.*, 2020, **27**, 29391–29407.
118 S. Hu, X. Qu, P. Li, F. Wang, Q. Li, L. Song, Y. Zhao and X. Kang, *Chem. Eng. J.*, 2018, **334**, 410–418.
119 X. Zou, R. Silva, A. Goswami and T. Asefa, *Appl. Surf. Sci.*, 2015, **357**, 221–228.
120 J. Cao, W. Zhang, X. Fu, H. Wang, S. Ma and Y. Liu, *Spectrochim. Acta, Part A*, 2020, **230**, 118040.
121 S. Hu, X. Qu, J. Bai, P. Li, Q. Li, F. Wang and L. Song, *ACS Sustainable Chem. Eng.*, 2017, **5**, 6863–6872.
122 Y. Wang, X. Zhou, W. Xu, Y. Sun, T. Wang, Y. Zhang, J. Dong, W. Hou, N. Wu, L. Wu, B. Zhou, Y. Wu, Y. Du and W. Zhong, *Appl. Catal., A*, 2019, **582**, 117118.
123 Z. Wang, J. Xu, H. Zhou and X. Zhang, *Rare Met.*, 2019, **38**, 459–467.
124 F. Qian, J. Wang, S. Ai and L. Li, *Sens. Actuators, B*, 2015, **216**, 418–427.
125 A. Kumar, R. K. Yadav, N. J. Park and J. O. Baeg, *ACS Appl. Nano Mater.*, 2018, **1**, 47–54.
126 Y. Rangraz, F. Nemati and A. Elhampour, *Appl. Surf. Sci.*, 2020, **507**, 145164.
127 Y. Wang, S. Hu, Q. Li, G. Gu, Y. Zhao, H. Liang and W. Li, *RSC Adv.*, 2018, **8**, 36903–36909.
128 M. Wang, Y. Zeng, G. Dong and C. Wang, *Chin. J. Catal.*, 2020, **41**, 1498–1510.
129 J. Hong, D. K. Hwang, R. Selvaraj and Y. Kim, *J. Ind. Eng. Chem.*, 2019, **79**, 473–481.
130 C. Zhang, J. Bai, L. Ma, Y. Lv, F. Wang, X. Zhang, X. Yuan and S. Hu, *Diamond Relat. Mater.*, 2018, **87**, 215–222.
131 M. Zhou, G. Dong, F. Yu and Y. Huang, *Appl. Catal., B*, 2019, **256**, 117825.
132 Y. Wang, Y. Li, X. Bai, Q. Cai, C. Liu, Y. Zuo, S. Kang and L. Cui, *Catal. Commun.*, 2016, **84**, 179–182.
133 Y. Wang, Y. Wang, Y. Li, H. Shi, Y. Xu, H. Qin, X. Li, Y. Zuo, S. Kang and L. Cui, *Catal. Commun.*, 2015, **72**, 24–28.
134 H. Che, C. K. Ngaw, P. Hu, J. Wang, Y. Li, X. Wang and W. Teng, *J. Alloys Compd.*, 2020, **849**, 156440.
135 J. Li, B. Zhang, Q. Song, X. Xu and W. Hou, *Ceram. Int.*, 2020, **46**, 14178–14187.
136 R. Zhang, A. Zhang, Y. Cao, S. Wang, F. Dong and Y. Zhou, *Chem. Eng. J.*, 2020, **401**, 126028.
137 Y. Wang, Y. Zhang, S. Zhao, Z. Huang, W. Chen, Y. Zhou, X. Lv and S. Yuan, *Appl. Catal., B*, 2019, **248**, 44–53.
138 N. Wang, J. Wang, J. Hu, X. Lu, J. Sun, F. Shi, Z. Liu, Z. Lei and R. Jiang, *ACS Appl. Energy Mater.*, 2018, **1**, 2866–2873.
139 H. Li, Y. Xia, Z. Liang, G. Ba and W. Hou, *ACS Appl. Energy Mater.*, 2020, **3**, 377–386.
140 Z. Liang, Y. Xia, G. Ba, H. Li, Q. Deng and W. Hou, *Catal. Sci. Technol.*, 2019, **9**, 6627–6637.
141 R. Ding, S. Cao, H. Chen, F. Jiang and X. Wang, *Colloids Surf., A*, 2019, **563**, 263–270.
142 W. Iqbal, B. Yang, X. Zhao, M. Rauf, I. M. A. Mohamed, J. Zhang and Y. Mao, *Catal. Sci. Technol.*, 2020, **10**, 549–559.
143 X. Hu, W. Zhang, Y. Yong, Y. Xu, X. Wang and X. Yao, *Appl. Surf. Sci.*, 2020, **510**, 145413.
144 Y. Huang, Q. Yan, H. Yan, Y. Tang, S. Chen, Z. Yu, C. Tian and B. Jiang, *ChemCatChem*, 2017, **9**, 4083–4089.
145 Y. Guo, T. Chen, Q. Liu, Z. Zhang and X. Fang, *J. Phys. Chem. C*, 2016, **120**, 25328–25337.
146 Q. Han, C. Hu, F. Zhao, Z. Zhang, N. Chen and L. Qu, *J. Mater. Chem. A*, 2015, **3**, 4612–4619.
147 T. S. Bui, P. Bansal, B. K. Lee, T. Mahvelati-Shamsabadi and T. Soltani, *Appl. Surf. Sci.*, 2020, **506**, 144184.
148 D. Long, W. Chen, S. Zheng, X. Rao and Y. Zhang, *Ind. Eng. Chem. Res.*, 2020, **59**, 4549–4556.
149 S. K. Kuila, D. K. Gorai, B. Gupta, A. K. Gupta, C. S. Tiwary and T. K. Kundu, *Chemosphere*, 2021, **268**, 128780.
150 T. Pan, D. Chen, J. Fang, K. Wu, W. Feng, X. Zhu and Z. Fang, *Mater. Res. Bull.*, 2020, **125**, 110812.
151 K. Wu, D. Chen, S. Lu, J. Fang, X. Zhu, F. Yang, T. Pan and Z. Fang, *J. Hazard. Mater.*, 2020, **382**, 121027.
152 Y. Xie, S. Peng, Y. Feng and D. Wu, *Chemosphere*, 2020, **239**, 124612.
153 N. Masunga, B. B. Mamba and K. K. Kefeni, *Colloids Surf., A*, 2020, **602**, 125107.
154 M. Wang, P. Guo, Y. Zhang, C. Lv, T. Liu, T. Chai, Y. Xie, Y. Wang and T. Zhu, *J. Hazard. Mater.*, 2018, **349**, 224–233.
155 J. Zhou, H. Luo, R. Ding, X. Cao, X. Zhou, Q. Chen and F. Jiang, *Colloids Surf., A*, 2020, **585**, 123853.
156 G. Li, B. Wang, J. Zhang, R. Wang and H. Liu, *Chem. Eng. J.*, 2020, **391**, 123500.
157 G. Zeng, M. Duan, Y. Xu, F. Ge and W. Wang, *Spectrochim. Acta, Part A*, 2020, **241**, 118649.
158 C. Li, Y. Wang, C. Li, S. Xu, X. Hou and P. Wu, *ACS Appl. Mater. Interfaces*, 2019, **11**, 20770–20777.
159 C. Gervais, E. Framery, C. Duriez, J. Maquet, M. Vaultier and F. Babonneau, *J. Eur. Ceram. Soc.*, 2005, **25**, 129–135.
160 D. J. Heldebrant, A. Karkamkar, N. J. Hess, M. Bowden, S. Rassat, F. Zheng, K. Rappe and T. Autrey, *Chem. Mater.*, 2008, **20**, 5332–5336.
161 J. Luo, X. Kang, Z. Fang and P. Wang, *Dalton Trans.*, 2011, **40**, 6469–6474.
162 Z. Huang, F. Li, B. Chen and G. Yuan, *Catal. Sci. Technol.*, 2014, **4**, 4258–4264.
163 Y. Wang, M. K. Bayazit, S. J. A. Moniz, Q. S. Ruan, C. C. Lau, N. Martsinovich and J. Tang, *Energy Environ. Sci.*, 2017, **10**, 1643–1651.

164 E. Han, Y. Li, Q. Wang, W. Huang, L. Luo, W. Hu and G. Huang, *J. Mater. Sci. Technol.*, 2019, **35**, 2288–2296.
165 E. B. Azimi, A. Badiei and J. B. Ghasemi, *Appl. Surf. Sci.*, 2019, **469**, 236–245.
166 S. Tang, Z. Fu, Y. Li and Y. Li, *Appl. Catal., A*, 2020, **590**, 117342.
167 J. Su, Y. Zhao and J. Xi, *Electrochim. Acta*, 2018, **286**, 22–28.
168 B. Amanulla, K. N. Perumal and S. K. Ramaraj, *Sens. Actuators, B*, 2019, **281**, 281–287.
169 Q. Zhang, Y. Liu, Y. Nie, Y. Liu and Q. Ma, *Anal. Chem.*, 2019, **91**, 13780–13786.
170 H. Han, G. Ding, T. Wu, D. Yang, T. Jiang and B. Han, *Molecules*, 2015, **20**, 12686–12697.
171 L. Muniandy, F. Adam, A. R. Mohamed, A. Iqbal and N. R. A. Rahman, *Appl. Surf. Sci.*, 2017, **398**, 43–55.
172 A. Liu, R. M. Wentzcovitch and M. L. Cohen, *Phys. Rev. B: Condens. Matter*, 1989, **39**, 1760–1765.
173 T. Kokulnathan and T. J. Wang, *Composites, Part B*, 2019, **174**, 106914.
174 S. Sarkar, N. Kamboj, M. Das, T. Purkait, A. Biswas and R. S. Dey, *Inorg. Chem.*, 2020, **59**, 1332–1339.
175 K. Mori, T. Murakami and H. Yamashita, *ACS Appl. Nano Mater.*, 2020, **3**, 10209–10217.
176 J. Deng, Q. Zhang, X. Lv, D. Zhang, H. Xu, D. Ma and J. Zhong, *ACS Energy Lett.*, 2020, **5**, 975–993.
177 M. Li, B. Wang, M. Yang, Q. Li, D. G. Calatayud, S. Zhang, H. Wang, L. Wang and B. Mao, *Sep. Purif. Technol.*, 2020, **239**, 116515.
178 Z. Luo, M. Zhou and X. Wang, *Appl. Catal., B*, 2018, **238**, 664–671.
179 D. H. Park, K. S. Lakhi, K. Ramadass, M. K. Kim, S. N. Talapaneni, S. Joseph, U. Ravon, K. Al-Bahily and A. Vinu, *Chemistry*, 2017, **23**, 10753–10757.
180 G. P. Mane, S. N. Talapaneni, K. S. Lakhi, H. Ilbeygi, U. Ravon, K. Al-Bahily, T. Mori, D. H. Park and A. Vinu, *Angew. Chem., Int. Ed.*, 2017, **56**, 8481–8485.
181 Y. Zhang, T. Mori, L. Niu and J. Ye, *Energy Environ. Sci.*, 2011, **4**, 4517–4521.
182 C. Dong and L. Vayssieres, *Chemistry*, 2018, **24**, 18356–18373.
183 J. Zhong, H. Zhang, X. Sun and S. T. Lee, *Adv. Mater.*, 2014, **26**, 7786–7806.
184 K. Kvande, D. K. Pappas, E. Borfecchia and K. A. Lomachenko, *ChemCatChem*, 2020, **12**, 2385–2405.
185 Y. Zhang, S. Jiang, W. Song, P. Zhou, H. Ji, W. Ma, W. Hao, C. Chen and J. Zhao, *Energy Environ. Sci.*, 2015, **8**, 1231–1236.
186 H. Chang, Y. Fu, W. Lee, Y. Lu, Y. Huang, J. Chen, C. Chen, W. Chou, J. Chen, J. F. Lee, S. Shen and C. Dong, *Nanotechnology*, 2018, **29**, 064002.
187 F. Hu, H. Wang, Y. Zhang, X. Shen, G. Zhang, Y. Pan, J. T. Miller, K. Wang, S. Zhu, X. Yang, C. Wang, X. Wu, Y. Xiong and Z. Peng, *Small*, 2019, **15**, 1901020.
188 L. Zhang, J. Ran, S. Qiao and M. Jaroniec, *Chem. Soc. Rev.*, 2019, **48**, 5184–5206.
189 K. Jiang, S. Siahrostami, A. J. Akey, Y. Li, Z. Lu, J. Lattimer, Y. Hu, C. Stokes, M. Gangishetty, G. Chen, Y. Zhou, W. Hill, W. Cai, D. Bell, K. Chan, J. K. Norskov, Y. Cui and H. Wang, *Chem*, 2017, **3**, 950–960.
190 C. Asokan, L. DeRita and P. Christopher, *Chin. J. Catal.*, 2017, **38**, 1473–1480.
191 T. G. Lach, M. J. Olszta, S. D. Taylor, K. H. Yano, D. J. Edwards, T. S. Byun, P. H. Chou and D. K. Schreiber, *J. Nucl. Mater.*, 2021, **549**, 12.
192 I. M. Hill, S. Hanspal, Z. D. Young and R. J. Davis, *J. Phys. Chem. C*, 2015, **119**, 9186–9197.
193 H. Zhang, X. Han, H. Yu, Y. Zou and X. Dong, *Sep. Purif. Technol.*, 2019, **226**, 128–137.
194 S. Le, T. Jiang, Q. Zhao, X. Liu, Y. Li, B. Fang and M. Gong, *RSC Adv.*, 2016, **6**, 38811–38819.
195 R. Li, J. Huang, M. Cai, J. Huang, Z. Xie, Q. Zhang, Y. Liu, H. Liu, W. Lv and G. Liu, *J. Hazard. Mater.*, 2020, **384**, 121435.
196 P. Raizada, A. Sudhaik, P. Singh, P. Shandilya, P. Thakur and H. B. Jung, *Arabian J. Chem.*, 2020, **13**, 3196–3209.
197 G. Dong, P. Qiu, F. Meng, Y. Wang, B. He, Y. Yu, X. Liu and Z. Li, *Chem. Eng. J.*, 2020, **384**, 123330.
198 P. Raizada, A. Sudhaik, P. Singh, P. Shandilya, A. K. Saini, V. K. Gupta, J. H. Lim, H. Jung and A. Hosseini-Bandegharaei, *Sep. Purif. Technol.*, 2019, **212**, 887–900.
199 P. Babu, S. Mohanty, B. Naik and K. Parida, *ACS Appl. Energy Mater.*, 2018, **1**, 5936–5947.
200 W. M. A. El Rouby, A. E. A. Aboubakr, M. D. Khan, A. A. Farghali, P. Millet and N. Revaprasadu, *Sol. Energy*, 2020, **211**, 478–487.
201 B. Liu, L. Ye, R. Wang, J. Yang, Y. Zhang, R. Guan, L. Tian and X. Chen, *ACS Appl. Mater. Interfaces*, 2018, **10**, 4001–4009.
202 A. Mohammad, M. E. Khan and M. H. Cho, *J. Alloys Compd.*, 2020, **816**, 152522.
203 R. Zhu, Y. Zhang, J. Wang, C. Yue, W. Fang, J. Dang, H. Zhao and Z. Li, *Anal. Bioanal. Chem.*, 2019, **411**, 7137–7146.
204 A. Sakthivel, A. Chandrasekaran, S. Jayakumar, P. Manickam and S. Alwarappan, *J. Electrochem. Soc.*, 2019, **166**, B1461–B1469.
205 T. Kokulnathan and S. M. Chen, *ACS Appl. Mater. Interfaces*, 2019, **11**, 7893–7905.
206 R. Zhu, Y. Zhang, X. Fang, X. Cui, J. Wang, C. Yue, W. Fang, H. Zhao and Z. Li, *J. Mater. Chem. B*, 2019, **7**, 2320–2329.
207 J. Zou, D. Mao, A. Arramel, N. Li and J. Jiang, *Appl. Surf. Sci.*, 2020, **506**, 144672.
208 A. Hassani, P. Eghbali and O. Metin, *Environ. Sci. Pollut. Res. Int.*, 2018, **25**, 32140–32155.
209 N. Ertugay and F. N. Acar, *Appl. Surf. Sci.*, 2014, **318**, 121–126.
210 S. Kamal, G. T. Pan, S. Chong and T. C. K. Yang, *Processes*, 2020, **8**, 104.
211 X. Ren, Q. Wu, H. Xu, D. Shao, X. Tan, W. Shi, C. Chen, J. Li, Z. Chai, T. Hayat and X. Wang, *Environ. Sci. Technol.*, 2016, **50**, 9361–9369.
212 H. Xu, Z. Qu, C. Zong, W. Huang, F. Quan and N. Yan, *Environ. Sci. Technol.*, 2015, **49**, 6823–6830.
213 J. S. Taurozzi, M. Y. Redko, K. M. Manes, J. E. Jackson and V. V. Tarabara, *Sep. Purif. Technol.*, 2013, **116**, 415–425.